DESIGN AND CHARACTERISATION OF

ELECTROMAGNETIC BANDGAP FILTERS

Kai Herbertz

Imperial College London

Department of Electrical and Electronic Engineering

Optical and Semiconductor Devices Group

A thesis submitted for the degree of Doctor of Philosophy

September 2010

Abstract

Most signal processing / communications applications heavily rely on filters. For adaptive spectrum filtering and for applications that switch between sets of different filter implementations, it would be beneficial to utilize just one, tuneable band-pass filter.

In recent years, the study of metamaterials emerged as an area of scientific research due to the unique attributes of metamaterials. Metamaterials typically are artificial structures with properties not found in nature, for instance negative refraction indexes. Their feature sizes span a fraction of the wavelength corresponding to their frequency of operation. A sub group of metamaterials, the electromagnetic bandgap (EBG) structures, exhibit stopbands for electromagnetic waves irrespective of polarization or angle of incidence. EBG structures prominently achieved surface wave suppression to minimise cross talk between neighbouring devices and improving antenna efficiency by acting as a perfect magnetic conductor within a certain frequency range.

The thesis investigates the suitability of EBG structures for filter implementations. The goal is to provide a tuneable band-pass filter for adaptive spectrum filtering and communication applications. The bandgap of an infinite array of EBG cells is numerically determined. Based on those results, an EBG band-pass filter implementation on a printed circuit board (PCB) is designed, fabricated and characterized. Different tuning methods were incorporated into the PCB design to create a tuneable EBG band-pass filter. An EBG filter was built on a fused silica wafer, in order to shift the passband to higher frequencies.

Acknowledgements

The first person that not only deserves, but certainly has my gratitude is my supervisor Dr Stepan Lucyszyn. Thank you for giving me the chance to work on such an exciting and interesting topic. I greatly appreciate the helpful discussions and the occasional nudge to steer me back on course. The MMICs you've kindly provided, as well as the idea, proved to be invaluable for the success of the thesis. It has been a marvellous experience and I cherish and treasure every moment of it.

I thank my examiners Dr Kristel Fobelets and Prof. Izzat Darwazeh for pointing out those sections that needed further clarification, but which were in my blind spot.

My thanks to Prof. Richard Syms for giving me the opportunity to be a member of the Optical and Semiconductor Devices group.

All of my friends and colleagues have my thanks, who took the time to discuss aspects of my work or show me how to use equipment. In particular Dr Werner Karl, Dr Munir Ahmad, Dr Sunil Kumar, Robert Hergert, Dr Toby Hopf, Dr Joo Young Choi, Dr Oleksiy Sydoruk and Dr Michael Larsson all have my gratitude.

The time at the Optical and Semiconductor Devices group would not have been the same without my dear friends and colleagues. I fondly remember the good times with people, who have left, like Dr Ariel Lipson, Dr Li Zhao, Dr Wen Zhang, Dr Robert Maher and Dr Robert Juhasz to name a few; people, who are still there - Dr Yun Zhou and Nuradawiyah Zaidon - and the new arrivals Aifric Delahunty, Alexey Denisov and Emiljana Krali.

Strange enough the librarians hardly get any mention in the acknowledgements, so here is my attempt to change that - Ellen Haigh, thank you very much for considering my book purchase recommendations and for always being friendly and supportive.

Last, but most definitely not least, I am grateful to my family for their limitless patience and support: Dr Ingetraud Herbertz, Dr Georg Herbertz, Dr Chiara Manfletti and Dr Armin Herbertz.

Diese Doktorarbeit ist meinen Eltern gewidmet.

Declaration of Originality

I hereby declare that this thesis is my own work and effort. Where other sources of information have been used, they have been acknowledged.

Kai Herbertz

August 2010

Contents

List of Figures

List of Tables

Glossary

ADS	Agilent's Advanced Design System

AMC	artificial magnetic conductor

AMICOM	Advanced MEMS for RF and Millimeter Wave Communications

DC	direct current

DNG	double negative material

EBG	electromagnetic bandgap

EM	electromagnetic

FDFD	finite difference frequency domain

FDTD	finite difference time domain

FEM	finite element method

FSS	frequency selective surfaces

HFSS™	high frequency structure simulator (software)

HRS	high resistive silicon

IPSVD	interdigitated planar Schottky varactor diode

ITC-irst	Instituto Trentino di Cultura - Il Centro per la ricerca scientifica e tecnologica (centre for scientific and technological research located in Italy)

MEMS	micro-electro-mechanical systems

MMIC	monolithic microwave integrated circuits

MoM	method of moments

MPW	multi project wafer

PBG	photonic bandgap

PCB	printed circuit board

PEC   perfect electric conductor

PMC   perfect magnetic conductor

Qu   unloaded quality

RF   radio frequency

SEM   scanning electron microscope

SMA   subminiature version A

SRR   split ring resonator

TM   transverse magnetic

UC   uniplanar compact

VTT   Valtion Teknillinen Tutkimuskeskus (governmental technical research

             centre of Finland)

1 Introduction

1.1 Motivation and Goals

Electronic filters are widely used in communications and signal processing. In order to avoid switching between different passive filter arrangements or for certain applications like adaptive spectrum filtering, it will be beneficial to employ tuneable filters.

In recent years, the search for artificial materials, specifically metamaterials and electromagnetic bandgap (EBG) structures, has attracted world wide interest from researchers. Among the various uses of EBG structures, their suitability as filters has already been demonstrated.

The thesis seeks to contribute to the research of EBG structures. To this end, a different approach for the implementation of filters with EBGs is investigated. The knowledge gain is further applied to create tuneable EBG filters with the intention of solving the demand for tuneable filters that was mentioned above.

1.2 Electromagnetic Bandgap Structures

EBG structures are considered to be a sub-class of metamaterials. The term metamaterials encompasses various periodic structures with properties that do not exist in nature. There are several different classes of metamaterials. Engheta and Ziolkowski divided their book on metamaterials into the single- and double-negative material class and the EBG structured metamaterial class [1]. In 1968, Veselago was the first to propose the existence of left handed materials and provide a theoretical analysis [2]. Left handed materials are also called double negative materials (DNGs) due to their properties: DNGs exhibit a negative permittivity ε and a negative permeability μ. The

actual realization of metamaterials came about some decades later. Prominent work includes John Pendry's papers on split ring resonator (SRR) metamaterial structures [3]. Frequency selective surfaces (FSS), EBGs and metamaterials are all periodic structures. Depending on the type of structure, the periodicity in relation to the guided wavelength λ_g is of a different order of magnitude: The period p of metamaterials is significantly smaller than the guided wavelength λ_g, whereas the period for EBGs is of the order of half a guided wavelength: $p \sim \lambda_g / 2$ [4]. As their names suggest, an EBG exhibits a specific frequency characteristic in its transmittance and / or reflectance properties, while the more general FSS may also alter other aspects like polarity or group delay.

Electromagnetic (EM) bandgap structures derive their name from an analogy to solid-state electronic bandgap structures. With the latter, there are certain energy bands that electrons can occupy and forbidden bands that cannot be occupied. With EBGs, the forbidden bands pertain to energy levels that photons cannot occupy. Hence, EM waves with a frequency inside the forbidden band cannot propagate through the EBG material, irrespective of their angle of incidence [5].
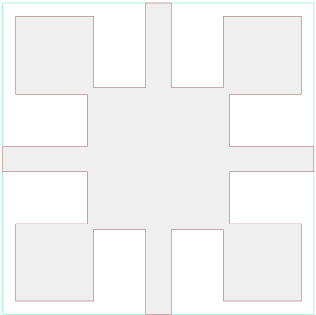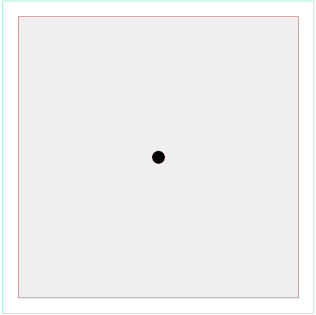
EBGs were first reported for structures at optical wavelengths in 1987 [6]. At that time they were referred to as photonic bandgap (PBG) structures or photonic crystals. Over the intervening years, artificial structures have been engineered at much higher wavelengths.
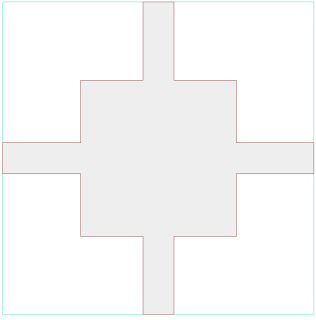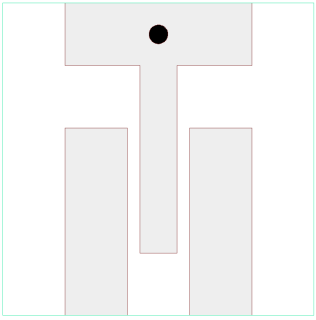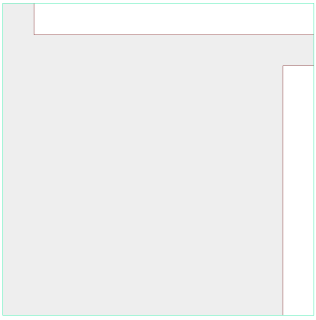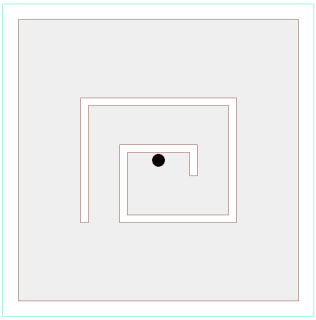
Initially, 3D metallic structures in the microwave frequency range were investigated [7], before the focus shifted to metallodielectric planar structures in the late 1990s.
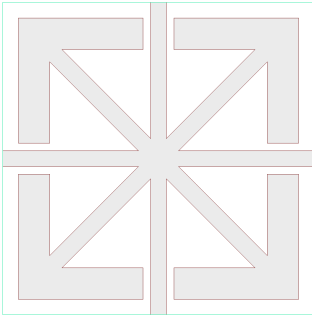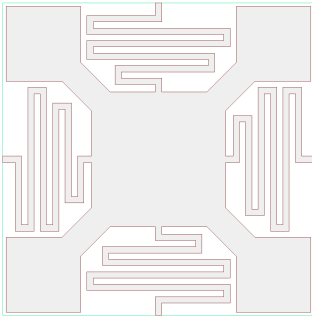
Planar EBGs are of particular interest at microwave frequencies, due to ease of fabrication. These EBGs are usually only periodic in a 2D plane and do not exhibit a bandgap for all angles of incidence of an EM wave, but just for all angles in that one

plane. Within the group of planar EBGs, the uniplanar compact EBG (UC-EBG) [8] and the mushroom type EBG [9] are of particular importance. The compactness of EBGs is determined by dividing the physical periodicity p with the wavelength λ of the bandgap centre frequency. The following Table 1.1 lists different geometries of EBG structures, the year of publication, the publication reference, the compactness as well as the bandgap. In the "structure" column, the plan view of only one cell of an EBG array is shown. Black circles indicate vias.

Table 1.1 Planar EBGs

Structure (one unit cell)	Year	Reference	p / λ	Bandgap (GHz)	Remark
	1999	[10]	0.122	10.9-13-5	uniplanar compact EBG. This configuration serves as starting point.
	1999	[9]	0.096	10-14	mushroom EBG

Structure (one unit cell)	Year	Reference	p / λ	Bandgap (GHz)	Remark
	2001	[11]	-	-	
	2004	[12]	0.07	4.61-5.22	
	2004	[13]	0.189	1.8-5.3	
	2005	[14]	0.048	2.07-2.34	

Structure (one unit cell)	Year	Reference	p / λ	Bandgap (GHz)	Remark
	2006	[15]	0.11	4.1-5.0	
	2008	[16]	0.11	2.26-4.53	Structure from this work, based on UC-EBG.

Initially it was stated that the period of EBGs is in the order of half a guided wavelength. At a guided wavelength corresponding to the centre frequency of the bandgap, this would relate to a compactness of 0.5. With the introduction of the UC-EBG, compact structures with $p / \lambda < 0.5$ were investigated, as shown in Table 1.1.

1.3 Applications of Electromagnetic Bandgap Structures

As an example of possible applications, EBGs could be used to improve the efficiency of antennas [17], due to the suppression of surface and substrate waves, which are the predominant loss mechanisms. Furthermore, the EBGs can function as an artificial magnetic conductor (AMC) at a certain EM wavelength [18]. A metal surface, as an approximation of a perfect electric conductor (PEC), has a voltage wave reflection coefficient of -1, which causes a reflection and a phase shift of 180 degrees to the incident EM wave. With an artificial magnetic conductor, as an approximation to a perfect magnetic conductor (PMC), there is an in-phase reflection. Due to destructive

interference, the PEC is undesirable as a ground plane for microstrip antennas. Having a PMC with a voltage wave reflection coefficient of +1 underneath a microstrip antenna increases the antenna's efficiency. While the drawback of the reflection coefficient of a PEC can be offset by a spacing of $\lambda/4$ between the antenna and the ground plane [9], the problem of surface waves still persist for PEC ground planes.

Another advantage of EBGs is the integration of components. Usually the required high dielectric constant of the substrate needed for a high level of integration would be detrimental for microstrip antennas. However, by using an EBG, the antenna could be shielded from the substrate, enabling it to be integrated with other components on the same substrate [10]. Similarly, EBGs can be utilised to reduce crosstalk between neighbouring components on a chip [10]. The radiation pattern of antennas can be changed with EBG structures [19]. Some research has been carried out on altering waveguides via EBGs [20],[21]. Another important point about EBGs is the idea of introducing defects into the structure in order to tweak its properties, similar to doping of semiconductors [5]. EBG structures could be used to enhance other radio frequency (RF) applications like attenuators, cavity resonators, filters, etc.

The thesis investigates a modified UC-EBG cell and filter implementations based on an array of such EBG cells. For that reason, other filter designs based on EBGs are of interest. In the late 1990s and early 2000s the EBG filter implementations consisted of a microstrip transmission line with an EBG patterned ground plane. Early designs consisted of circles that were etched into the ground plane [22]. A similar implementation uses cascaded sections of varying radii [23]. In addition to varying the radii of the circle, the microstrip line can also be changed to contain sections of different widths in order to influence the filter performance [24]. EBG filters like this have been

designed with different EBG structures, for instance with the UC-EBG [25],[26] or with a resonant slot, in the shape of two connected spiral EBGs [27].

1.4 Thesis Structure

The thesis is structured as follows: Chapter 2 provides an overview of the different methods to characterise EBG structures. The properties of the UC-EBG are shown. Chapter 3 introduces the modified UC-EBG of this thesis. Chapter 4 describes how prototype EBG filters, made of arrays of the modified UC-EBG cell from Chapter 3, were created. The process flow starts at the design, moves to the modelling and 3D simulations, before reaching the fabrication and measurement stage. A 2D equivalent circuit model of the filter is presented as well. Chapter 5 discusses the results of a monolithic implementation of the EBG array. The penultimate chapter explores different methods for tuning the devices from Chapters 4 and 5. Finally, Chapter 7 summarizes the results of the previous chapters and highlights areas that might benefit from further work.

2 Theoretical Background

This chapter illuminates the relation of the Brillouin zone to the dispersion diagram of EBG structures. Different methods of analysing EBG structures are discussed.

2.1 Important Planar Electromagnetic Bandgap Configurations

Although many different planar EBG configurations exist, the two most important ones are the UC-EBG and the mushroom EBG. Many of the other EBGs are variations of these two, which is why it is important to describe their properties. The EBG cell examined in this thesis is based on the UC-EBG and is referred to as modified UC-EBG throughout.

2.1.1 The Uniplanar Compact Electromagnetic Bandgap Cell

The conventional UC-EBG cell has a shunt capacitance C_p, and is coupled to other UC-EBG cells by a series inductor, L_s, in parallel with two series capacitors, C_s. Figure 2.1 (a) shows the plan view of a 3 x 3 cell array of the conventional UC-EBG cell. Such arrays are typically produced on printed circuit boards (PCB). The PCB is a laminate, consisting of a insulating substrate between two metal sheets. The bottom metal sheet usually serves as a ground plane. The top metal sheet is patterned. In Figure 2.1 (a), grey areas indicate the structure's patterned top metal layer. White areas represent the substrate material without metal. The cell in the centre of the array shows and clarifies the position of the equivalent circuit model components. The side view (not to scale) can be seen in Figure 2.1 (b).
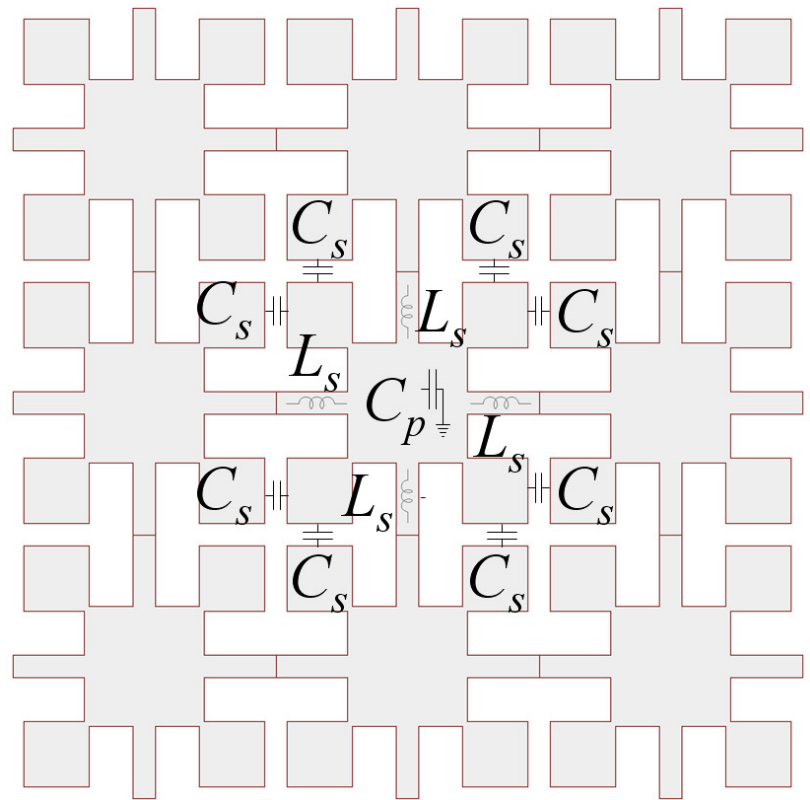
(a)
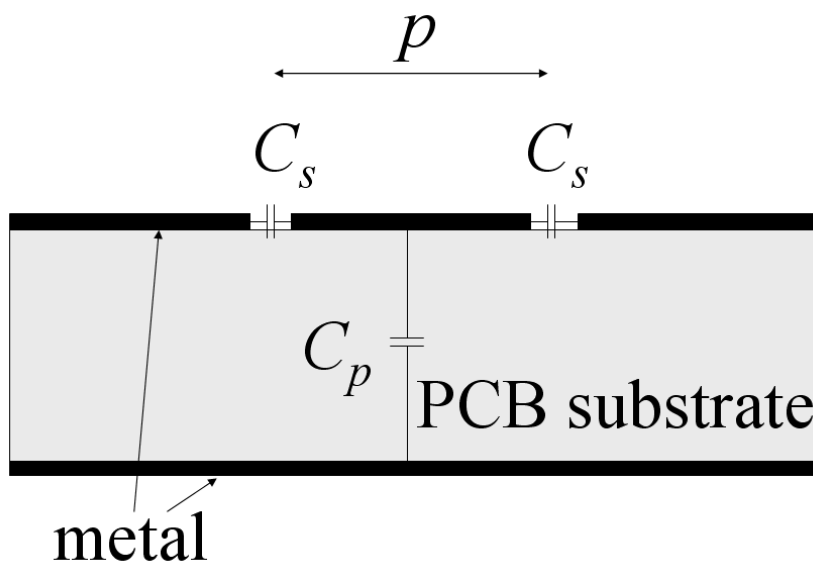
(b)

Figure 2.1 (a) Plan view of the conventional UC-EBG cell 3 x 3 array. (b) side view

(not to scale) of the conventional UC-EBG cell 3 x 3 array.

One of the advantages of the UC-EBG is its ease of fabrication, as it is a planar

structure without the need for vias [10].

2.1.2 Mushroom Electromagnetic Bandgap Cell

The mushroom EBG cell has a via in its centre that acts as a shunt inductance L_p. It is coupled to other mushroom EBG cells by series capacitors C_s. Figure 2.2 (a) shows the plan view of a 3 x 3 cell array of mushroom EBG cells. In Figure 2.2 (a), grey areas indicate the structure's patterned top metal layer. White areas represent the substrate material without metal. The side view (not to scale) can be seen in Figure 2.2 (b).

(a)

p

C_s C_s

L_p

metal PCB substrate

(b)
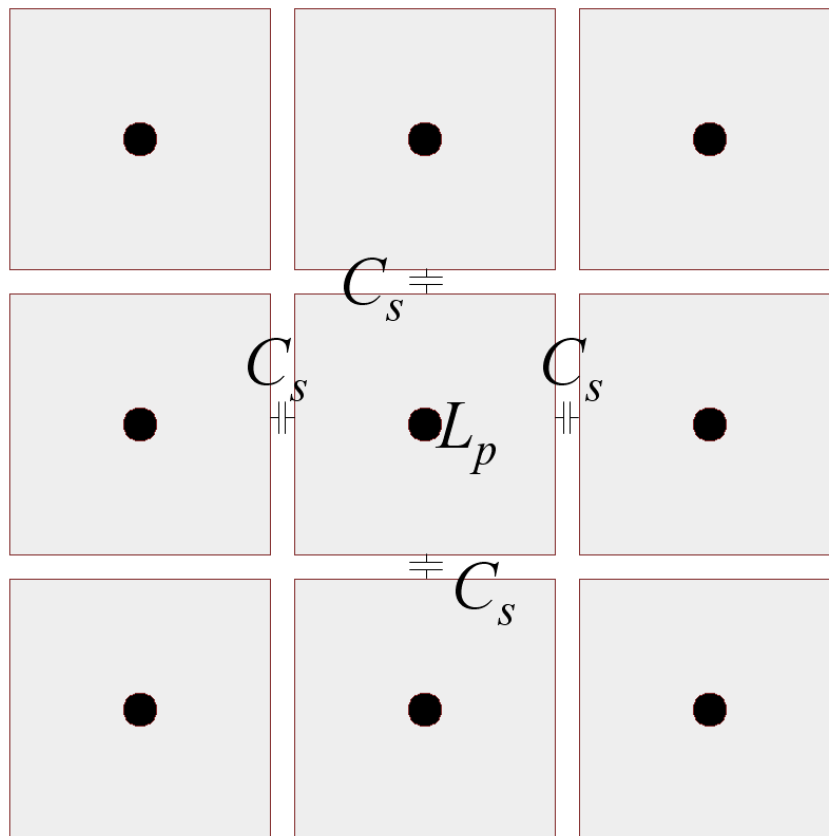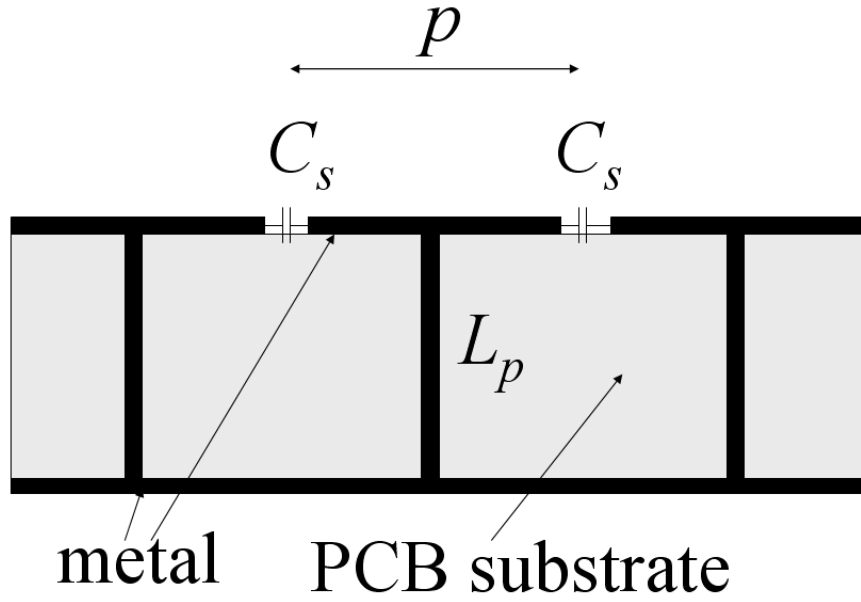
Figure 2.2 (a) Plan view of the mushroom EBG cell 3 x 3 array. (b) side view (not to scale) of the mushroom EBG cell 3 x 3 array.

2.2 Brillouin Zone

For the numerical computation of the band gap, explained in section 2.3, the concept of the Brillouin zone is of great importance. The analysis of EBGs and photonic crystals uses the same concepts and terminology as crystallography [28]. Therefore, this section explains what a Brillouin zone is, how it is constructed and how it relates to EBG structures.

As the thesis focuses on 2D EBG structures, the analysis is explained with 2D structures in mind. The same principles apply to 3D structures, though. In the introduction it was mentioned that EBGs are periodic structures. With 2D EBGs periodicity means that the EBG cells are tiled in an array. For the analysis of the bandgap, it is often assumed that the EBG array is of infinite length.

In a periodic structure, the behaviour of a wave outside of the first Brillouin zone is the same as inside the first Brillouin zone [29]: the exact location of a wave within the periodic structure is irrelevant, as there is a corresponding location in the first Brillouin zone that would have the same influence on the wave's propagation. For the purpose of setting up a simulation, this means that it is sufficient to analyse one unit cell or rather the first Brillouin zone around the lattice point, provided the correct boundary conditions have been chosen to mimick an infinite array.

In general the first Brillouin zone is simply referred to as Brillouin zone and the numbering second, third and so on is used for the Brillouin zones beyond the first Brillouin zone. The graphical construction of the Brillouin zones for a 2D lattice is done as follows [30]: from one point of the lattice, lines to other points of the lattice are drawn. In the middle of these lines and perpendicular to them, a line for a 2D lattice or a plane for a 3D lattice is constructed. These planes are referred to as Bragg planes.

Figure 2.3 shows the Bragg planes between the central lattice point and other lattice points. For example, the yellow circle in the middle of Figure 2.3 represents the centre of one EBG cell. The centres of the four nearest adjacent cells, vertically and horizontally, are marked as red circles. In between the yellow circle and each red circle is a red line, which is the Bragg plane.
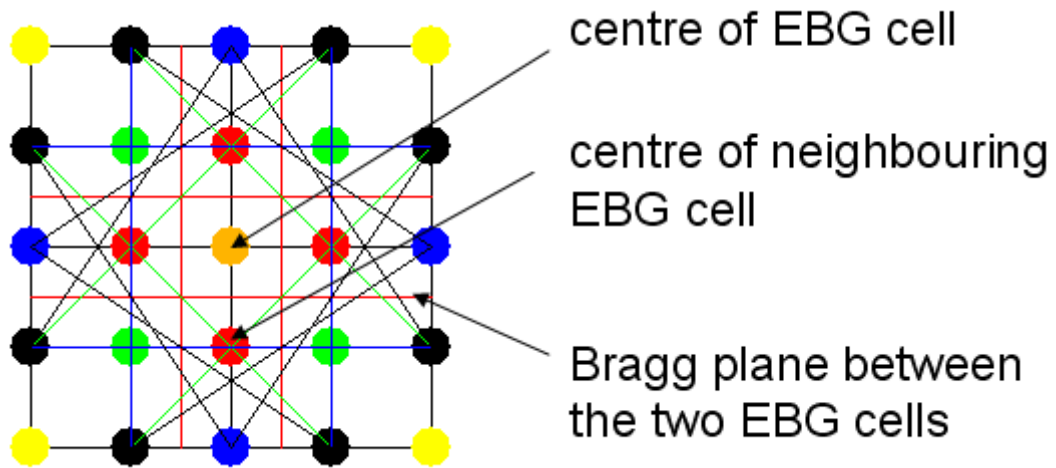
Figure 2.3 Construction of the Bragg planes in relation to the central lattice point [30].

The first Brillouin zone extends from the chosen point of the lattice to the Bragg planes. The area that is beyond the first Bragg plane, but walled in by Bragg planes as well, is the second Brillouin zone. Whenever a Bragg plane is crossed, a new Brillouin zone begins. This zone ends at the borders of the Bragg planes. Figure 2.4 shows an example of the first four Brillouin zones in a 2D square lattice. The colors correspond to the colors in Figure 2.3, for example the red Bragg planes between the central circle and the red circles of Figure 2.3 mark the borders of the red Brillouin zone shown in Figure 2.4.
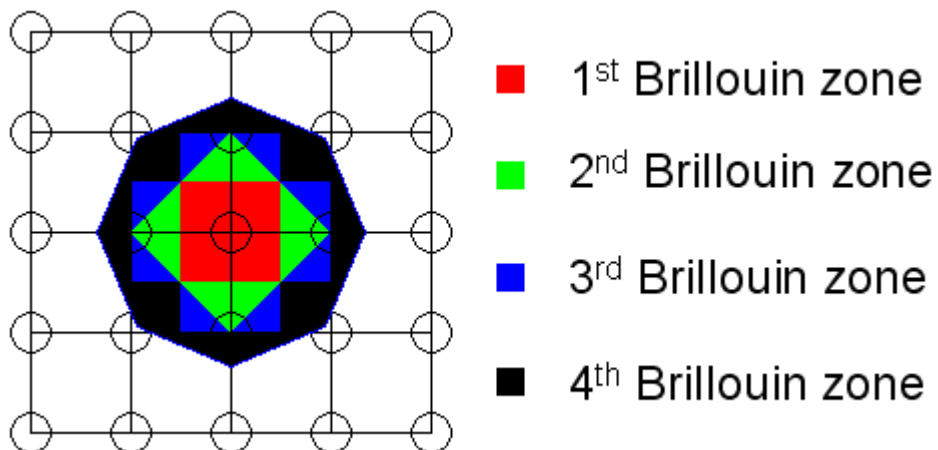
Figure 2.4 The first four Brillouin zones in a square lattice [30].

For a square lattice, the first Brillouin zone is a square and for a hexagonal lattice, the first Brillouin zone is a hexagon. Usually there is also symmetry in the Brillouin zone, so that the calculation of the dispersion diagram is along the lines connecting the critical points. Critical points are points of high symmetry [28]. The nomenclature for the cube is used for the square lattice as well. Γ denotes the centre of the Brillouin zone, X stands for a centre of a face and M is the centre of an edge. This region of symmetry within a Brillouin zone is called the irreducible Brillouin zone. For a square lattice, the irreducible Brillouin zone is triangle shaped.

2.3 Identifying the Bandgap

In order to visualize the bandgap, different methods exist. In the following sub sections, the reflection phase, the suspended microstrip line method, as well as the dispersion diagram are discussed. To obtain the dispersion characteristics of an EBG structure, an eigenmode solver for an infinite array needs to be used. Different types of algorithms may be used to solve Maxwell's equations in order to compute the dispersion diagram. Among those algorithms are finite difference frequency domain (FDFD), finite difference time domain (FDTD), method of moments (MoM) and the finite element method (FEM). The sub section about dispersion diagrams provides deeper insight into an FEM based process. Other approaches to construct the dispersion diagram from Maxwell's equations are available, for instance plane wave expansion method and rigorous coupled-wave analysis [31].

2.3.1 Reflection Phase

The reflection of a plane wave, which is impinging on a PEC surface, has a reflection phase of 180°. The reflection of a plane wave impinging on an EBG surface has a reflection phase that varies from +180° to -180° with increasing frequency of the plane

wave [32]. It was found experimentally that the frequency region between +90° and -90° coincides with the bandgap of the EBG [9].

2.3.2 Suspended Microstrip Line Method

Several papers [33]-[35] characterise the EBG structure by using the EBG array as a ground plane for a microstrip transmission line, which was suspended above the array. This method is very similar to the implementation of an EBG as a filter. The suspended microstrip line method is used to find the surface wave suppression characteristics of EBG structures. In the paper, the frequency range with insertion losses of less than -10 dB coincided with the bandgap [34].

2.3.3 Dispersion Diagram

Historically, the theory for wave propagation in periodic structures was solved analytically for simple periodic structures [36]. Today, the bandgap of even complex structures can be obtained by numerical means. To verify that the examined EBG structure exhibits a bandgap, the theoretical dispersion diagram was computed with the eigenmode solver within the Ansoft High Frequency Structure Simulator (HFSS™) software. The solution setup for the FEM based bandgap analysis has been previously described [37]. The eigenmode solver determines the resonant frequency for a given wavenumber k. This solution is not unique, which means that several propagation constants can exist at one frequency [32]. The results of these simulations can be seen in the next chapter about the structures examined in the thesis.

In order to simulate an infinite array, one unit cell (encapsulated by an air box) is modelled and periodic boundaries are set up along its sides. On top of the air box is a perfectly matched layer, which is terminated by a perfect electric conductor. This model of a periodic array with one unit cell corresponds to the Brillouin zone mentioned in

section 2.2. In a noteworthy paper [10], Coccioli et al. characterized a planar UC-EBG, which included dispersion diagrams. They also used the field distribution to identify the nature of the modes. The dispersion diagram of the UC-EBG is shown in Figure 2.5. Due to symmetry, the dispersion diagram was computed along the edges of the irreducible Brillouin zone, following the triangle with the points Γ, X and M.

While the branches from Γ to X and X to M are equidistant, the branch from M to Γ is longer. Consequently, the spacing between points increase in the M to Γ branch, as it contains the same amount of data points as the other branches. Although the dispersion diagram is presented as one continuous graph, it is composed of three graphs. Each of those graphs describes the dispersion characteristics of one of the three branches mentioned above.
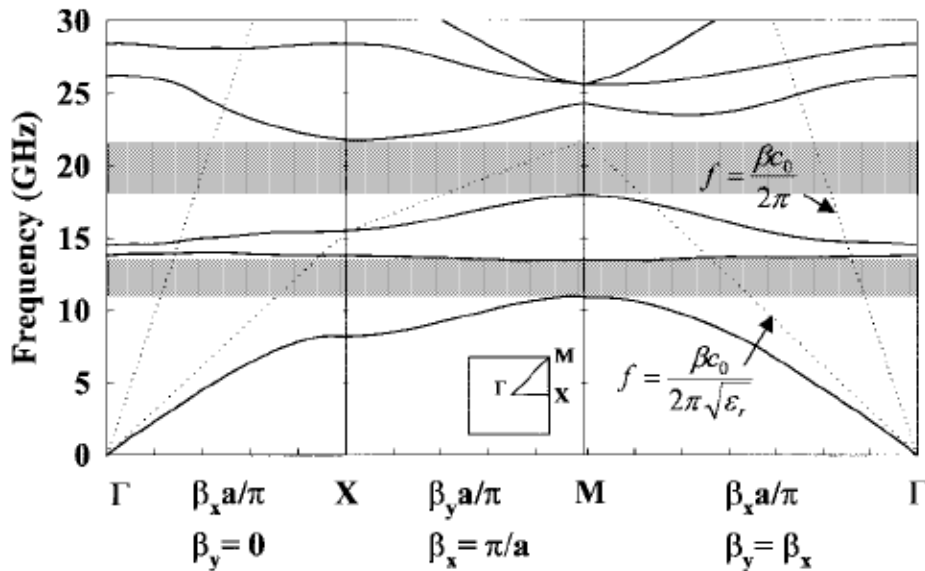
Figure 2.5 Computed dispersion diagram for a UC-EBG cell on a 635 µm thick substrate with relative permittivity $\varepsilon_r = 10.2$ [10].

In HFSS™, the eigenmode solver determines the complex resonant mode frequency of a structure $\widetilde{\omega}_0$ [38]. For each resonant mode frequency, the unloaded Qu-factor can be calculated as follows [38]:

31

$$Qu(|\widetilde{\omega}_0|) = \frac{1}{2}\sqrt{\left(\frac{\Re\{\widetilde{\omega}_0\}}{\Im\{\widetilde{\omega}_0\}}\right)^2 + 1} \qquad\qquad (2.1)$$

where $\Re\{\ \}$ and $\Im\{\ \}$ represent the real and imaginary parts, respectively, of the bracketed term. A low Qu-factor indicates high attenuation of the corresponding propagating mode. If these modes are sufficiently attenuated, the EM waves are quasi-evanescent and, thus, those frequency points can be ignored when determining the bandgap as they do not stand for propagating modes. This is the case when the real part is less than 10 times the imaginary part of the resonant frequency [37]. In terms of the unloaded Qu-factor, this cut-off point corresponds to Qu = 5.0, according to (2.1).

The data points with a low Qu-factor usually lie beyond the light line, which is a region that contains radiating modes rather than surface waves [9].

The light line shows the phase shift of a wave that is propagating in vacuum. For instance, a wave with a wavelength of 10 mm, which corresponds to the unit cell length, would exhibit a 360° phase shift. For different wavelengths, the phase shift would be (p / λ) x 360°, with p being the periodicity of the structure and λ being the wavelength. Substituting λ for c / f yields the following equation for the frequency in relation to the phase shift: $f =$ (phase shift / 360°) c / p. c is the speed of light in vacuum. For a dielectric material, the phase velocity is less than the speed of light. In those cases the speed of light divided by the square root of the effective relative permittivity needs to be used instead of c. In Figure 2.5, the light line and the line for the dielectric material is drawn as well.

2.4 Filters

This section is a brief overview of passive analogue electrical filters. Filter theory and the terms used in this section can be found in [39].

2.4.1 Filter Characteristics

There are four different filter characteristics regarding the signal attenuation in relation to frequency:

- low-pass filters attenuate signals at frequencies above their cutoff frequency.

- high-pass filters attenuate signals at frequencies below their cutoff frequency.

- band-pass filters attenuate signals at frequencies below their first cutoff frequency and above their second cutoff frequency.

- band-stop filters attenuate signals at frequencies above their first cutoff frequency and below their second cutoff frequency.

2.4.2 Filter Types

An ideal filter would have a rectengular frequency shape, switching from high attenuation outside of its passband to zero attenuation inside its passband region. However, ideal analogue filters do not exist. Filter implementations come in different types, depending on which property is being optimized. The two most famous filter types are:

- Butterworth filters, which are also called "maximally flat filters". Butterworth filters do not have ripples.

- Chebyshev filters have a faster cutoff than Butterworth filters, but contain ripples in either the passband or the stopband, depending on the implementation.

2.4.3 Filter Parameters

Beside the filter characteristic and the type, different other filter parameters exist. These parameters further describe the behaviour of the filter:

- the centre frequency

- 3dB bandwidth

- cutoff

- ripple

- order (roll off), the order is determined by the number of resonant pairs and in turn influences the roll off. Per order, the filter has a roll off of 20 dB / decade (or around 6 dB per octave).

- loss

Figure 2.6 shows the different parameters of a lossless 3rd order butterworth band-pass filter with a centre frequency of 3.5 GHz and a 3dB bandwidth of 2.2 GHz.
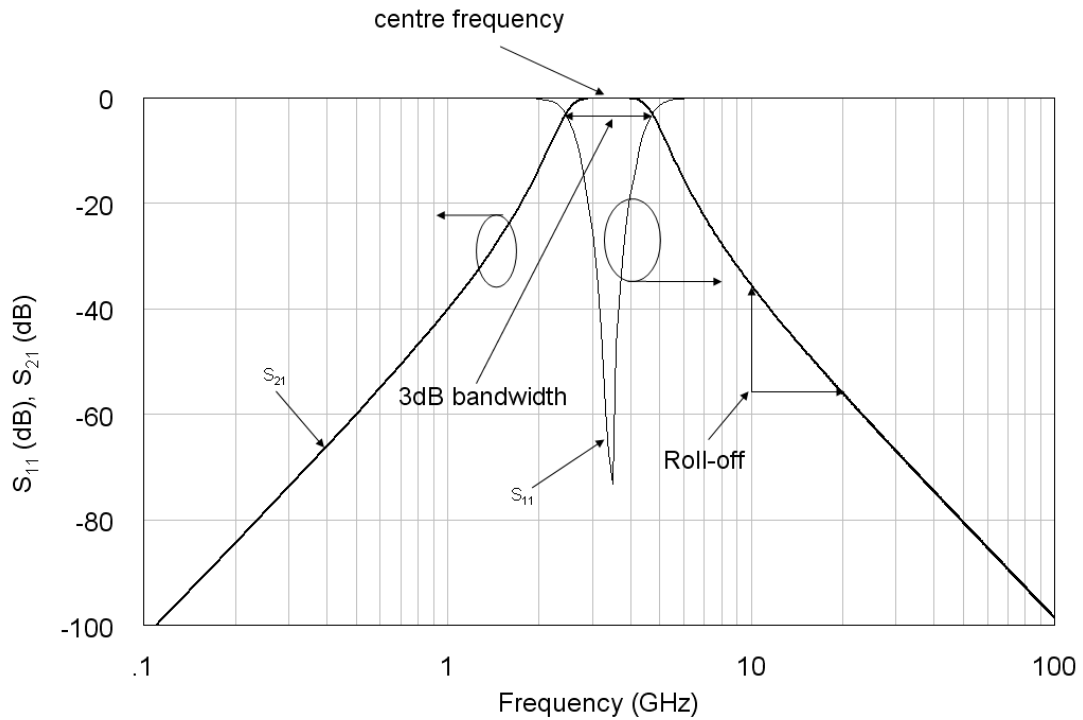
Figure 2.6 Filter Parameters.

At 10 GHz, the filter in Figure 2.6 has an insertion loss of -35.5 dB. At 20 GHz, it is at -56 dB. The roll off in that octave is around 20 dB, which is in line with the 6 dB per octave per filter order.

2.4.4 Example of a Band-pass Filter Equivalent Circuit Model

Different filter implementations exist, to produce the desired characteristics. The band-pass filter with the response shown in Figure 2.6 was created with the program rfsim99. Since it is a third order filter, it contains three resonant LC pairs. The equivalent circuit model for the filter can be seen in Figure 2.7.
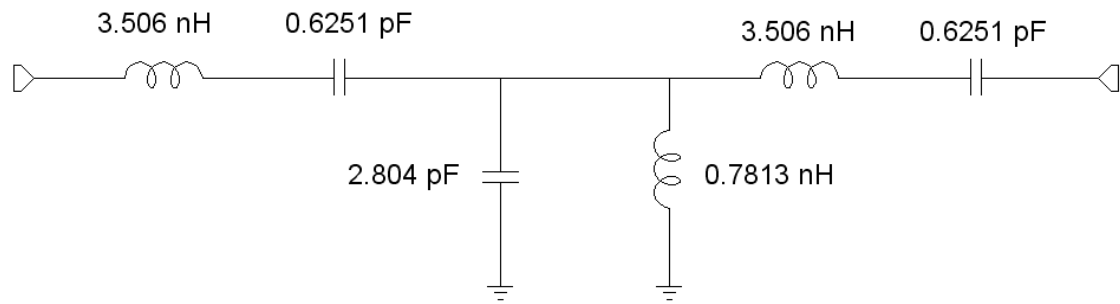
Figure 2.7 Equivalent circuit model of a 3rd order band-pass filter with centre frequency 3.5 GHz.

2.5 Summary

The properties of two important planar EBG structures were presented. One of the structures, the UC-EBG is of particular importance, because the work of this thesis is a continuation and modification of that design. Different methods for characterising EBG structures were presented. The most important tool to display the bandgap is the dispersion diagram. Since later chapters deal with the design and implementation of EBG filters, a brief overview of filter characteristics in general is given.

3 The Modified Uniplanar Compact Electromagnetic Bandgap Cell

The previous chapter highlighted the importance and attributes of the UC-EBG. That 2D EBG cell serves as a starting point for the new design investigated in this thesis, which is a modification of the UC-EBG. Whenever there is mention of the "modified UC-EBG", it refers to the structure examined in and unique to this thesis.

Two technologies for realizing a modified UC-EBG are presented in this thesis; one using low cost PCB and the other micromachined on a fused silica wafer.

3.1 Printed Circuit Board Implementation

Figure 3.1 shows the unit cell of the modified UC-EBG realised on PCB. The dimensions of the features were expressed in relation to the periodicity p. It can be seen that the inductances between cells have been increased by changing their associated geometry from a short straight wide line to a long meandered thin line. Initial designs that were subsequently discarded replaced the straight line with a meander that had sections of equal length. In order to utilise more space for the meanders, the rectangular patches on the sides were connected to the main patch by diagonal lines. With this change, the length of meander sections could further be increased at the cost of having sections of different lengths. Sections of different lengths make the inductance calculations slightly more complicated, which can be seen in section 3.1.1.2. For the inductance calculation, the meander sections are numbered from 1 to 13 and the direction of current is represented by arrows.

In the design shown, at the end of each meander, at the border to the adjacent cell, a via hole has been added. As a result, the inductive coupling between cells is removed and shunt inductance is added.
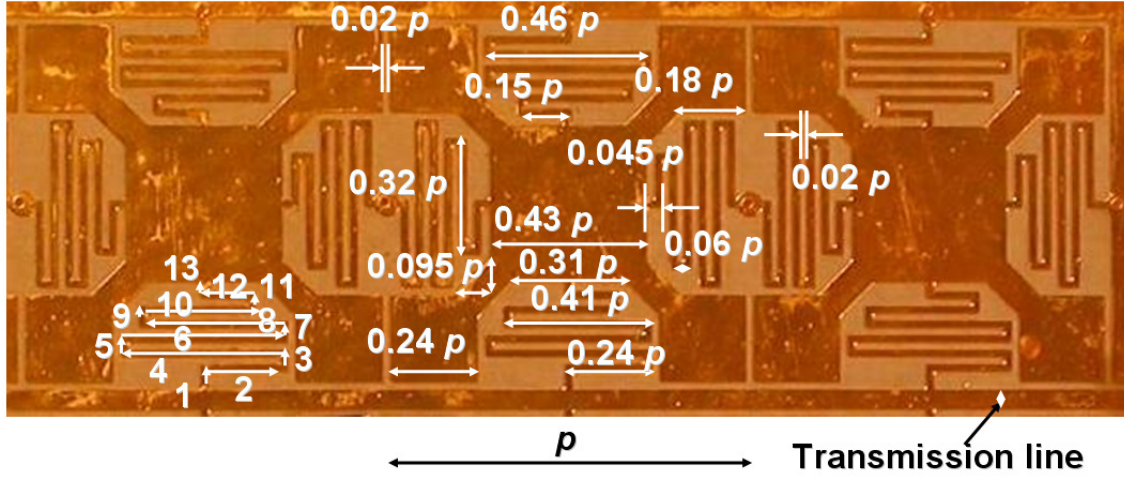
Figure 3.1 Plan view of a 3 x 1 array of the modified UC-EBG cell on PCB.

3.1.1.1 Capacitance Calculation

The capacitances were calculated with the well known formula for parallel plate capacitors:

$$C = \varepsilon_0 \varepsilon_r \frac{A}{d} \tag{3.1}$$

Where ε_0 is the permittivity in free space ($\varepsilon_0 \sim 8.854$ x 10^{-12} F / m), ε_r is the relative permittivity of the material in between the capacitor plates, A is the area of the plates and d is the distance between plates.

For the series capacitance C_s the area A_s = conductor thickness x 0.24 p, the distance $d_s = 0.02\ p$ and the dielectric between the parallel capacitors is air, with $\varepsilon_r \sim 1$. Thus, C_s = (8.854 x 10^{-12} F / m) x 1 x 18 μm x 12 = 1.9124 fF. Since both the area A_s and the distance d_s are dependent on the periodicity p, this capacitance value remains the same, irrespective of p. One exception is that as p decreases, the the effect of fringe

38

capacitances becomes more significant. For the modified UC-EBG cells examined here, the actual value of C_s would be larger than 1.9124 fF due to the fringe capacitances, but it would still be in the order of femto Farad.

The shunt capacitor C_p only takes the main part of the cell without the meanders into account for the calculation of the area. With the dimensions from Figure 3.1 (a) the area is calculated as $A_p \sim 0.4465\,p^2$. The distance is the thickness of the PCB, $d_p = 250$ μm. The dielectric is the circuit board material RF35 with $\varepsilon_r = 3.5$. Table 3.1 lists the different capacitance values for several periodicities p.

Table 3.1 Capacitance Values of the PCB EBG Cell

p [mm]	C_p [pF]	C_s [fF]
1	0.055346	1.9124
2.5	0.34591	1.9124
5	1.3837	1.9124
7.5	3.1132	1.9124
10	5.5346	1.9124
12.5	8.6479	1.9124
15	12.453	1.9124
17.5	16.95	1.9124
20	22.139	1.9124
22.5	28.019	1.9124
25	34.591	1.9124
27.5	41.856	1.9124
30	49.812	1.9124
55	167.42	1.9124

3.1.1.2 Inductance Calculation

The UC-EBG's inductance between cells consists of the self inductance of the straight conductor that connects two UC-EBG cells. In order to increase this inductance, the proposed change of the modified UC-EBG of this thesis, is to alter the geometry from a straight line into a meander. The sections of the meander each have self inductance and also exhibit mutual inductance between sections.

Calculations for planar inductors can be found in the PhD thesis of Dr Werner Karl [40]. The calculations there are based on the works of Grover [41] and Greenhouse [42].

The total inductance L_T is equal to the total self inductance L_0 plus the positive mutual inductance M_+ and minus the negative mutual inductance M_-:

$$L_T = L_0 + M_+ - M_-$$
(3.2)

The total self inductance L_0 is the sum of the self inductances of the conductor segments. The formula for self inductance L_x is given below:

$$L_0 = L_1 + L_2 + ... + L_n$$
(3.3)

$$L_x = 2l_x(\ln(\frac{2l_x}{w+t}) + 0.50049 + \frac{w+t}{3l_x})$$
(3.4)

In (3.4) l_x stands for the length of the inductor, w is the segment width and t is the segment thickness. These dimensions are in centimeters and the calculated inductance is in nanohenries.

The general equation for the mutual inductance M of two parallel conductors of equal length is as follows:

$$M = 2lQ$$
(3.5)

l is the length in cm and Q is called the mutual inductance parameter:

$$Q = \ln(\frac{l}{GMD} + \sqrt{1 + \frac{l^2}{GMD^2}}) - \sqrt{1 + \frac{GMD^2}{l^2}} + \frac{GMD}{l} \qquad (3.6)$$

If the current in both conductors flows into the same direction, then the mutual coupling is positive. If the directions of the currents oppose each other, then the mutual coupling is negative.

GMD stands for the geometric mean distance between the two conductor segments. It is roughly equivalent to the distance *d* between track centers. *GMD* can be calculated as follows:

$$\ln(GMD) = \ln(d) - ((\frac{1}{12}(\frac{d}{w})^2) + (\frac{1}{60}(\frac{d}{w})^4) +$$
$$(\frac{1}{168}(\frac{d}{w})^6) + (\frac{1}{360}(\frac{d}{w})^8) + (\frac{1}{660}(\frac{d}{w})^{10}) + ...) \qquad (3.7)$$

Greenhouse's paper [42] contains the formula for mutual inductance of conductor segments with different lengths, following the arrangement displayed in Figure 3.2.
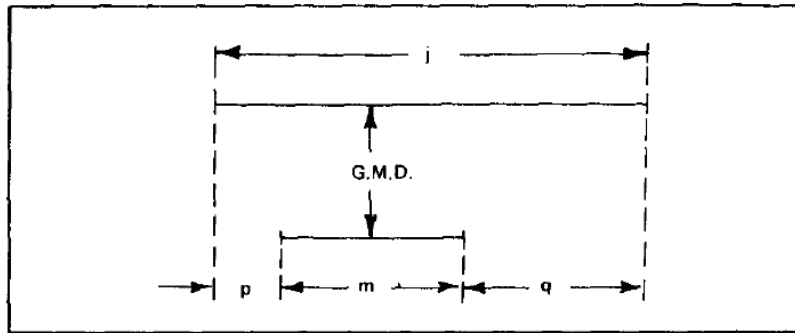
Figure 3.2 Two parallel-filament-geometry according to Greenhouse [42].

$$2M_{j,m} = +(M_{m+p} + M_{m+q}) - (M_p + M_q) \qquad (3.8)$$

The individual mutual inductances M_{m+p}, M_{m+q}, M_p, M_q are calculated from (3.5) and (3.6) by using the length of $(m+p)$, $(m+q)$, p and q respectively, instead of l.

Based on (3.8), Greenhouse listed two special cases. If $p = q$, (3.8) becomes (3.9):

$$M_{j,m} = M_{m+p} - M_p \qquad (3.9)$$

If $p = 0$, (3.8) becomes (3.10):

$$2M_{j,m} = +(M_m + M_{m+q}) - M_q \qquad (3.10)$$

With the direction of current and the lengths of the meander segments from Figure 3.1 (a) and the formulae mentioned in this chapter, the inductance of the meander was calculated. The matlab code for the calculation can be found in the appendix. Table 3.2 lists the total self inductance L_0, the self inductance if the meander were a straight line $L_{straight}$, the positive mutual inductance M_+, the negative mutual inductance M_- and the total Inductance L_T.

Table 3.2 Inductance Values of the PCB EBG Cell

p [mm]	L_0 [nH]	$L_{straight}$ [nH]	M_+ [nH]	M_- [nH]	L_T [nH]
1	1.4094	2.3198	0.79046	1.6404	0.55949
2.5	3.8689	6.1663	1.9762	4.101	1.744
5	8.0352	12.644	3.9523	8.2021	3.7854
7.5	12.218	19.139	5.9285	12.303	5.8429
10	16.405	25.638	7.9046	16.404	7.9051
12.5	20.594	32.138	9.8808	20.505	9.9692
15	24.784	38.64	11.857	24.606	12.034
17.5	28.974	45.143	13.833	28.707	14.1
20	33.166	51.646	15.809	32.808	16.166
22.5	37.357	58.149	17.785	36.909	18.233
25	41.548	64.652	19.762	41.01	20.299
27.5	45.74	71.156	21.738	45.112	22.366
30	49.932	77.659	23.714	49.213	24.433
55	91.852	142.7	43.475	90.223	45.104

3.1.2 Bandgap

The influence of the size of the meander and of the main capacitance on the centre frequency of the band gap will be explained in this section.

For the frequency range below 2 GHz, the cells that are connected to the microstrip transmission line in Figure 3.1 can be simplified to the equivalent circuit model shown in Figure 3.3 (a).

(a)   (b)
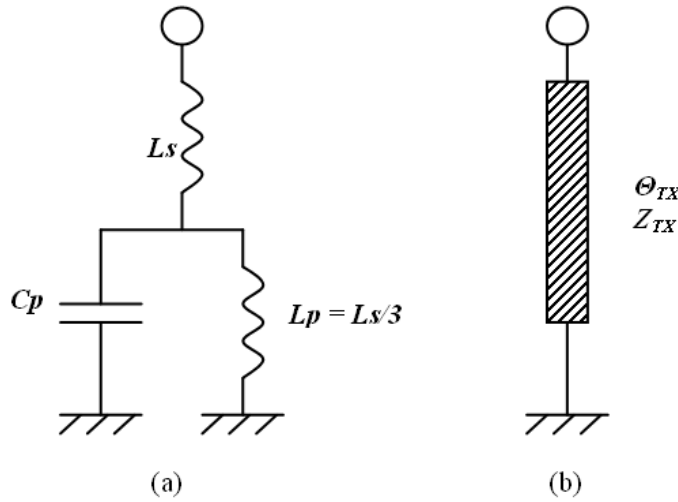
Figure 3.3 Equivalent circuit model for a cell in the first row: (a) low frequency; and (b) high frequency.

The low frequency driving-point impedance for this cell is given by the following expression:

$$Z(\omega) = j\omega L_s \frac{(4 - \omega^2 L_s C_p)}{(3 - \omega^2 L_s C_p)} \tag{3.11}$$

This means that the filter's low frequency lumped-element transmission zeros occur at the angular frequencies listed in (3.12) and (3.13). The transmission pole is at the angular frequency shown in (3.14). Therefore, this pole represents the parallel resonance of the three grounded series inductors with the shunt capacitance of the cell. It defines the position of the peak at 1.19 GHz in Figure 3.4. It is worth noting that the

43

relative spectral positions of the second transmission zero to transmission pole is fixed, since the term in (3.15) is constant.

$$\omega_{z1} = 0 \qquad (3.12)$$

$$\omega_{z2} = 2/\sqrt{L_s C_p} \qquad (3.13)$$

$$\omega_p = \sqrt{3/L_s C_p} \qquad (3.14)$$

$$\omega_{z2}/\omega_p = 2/\sqrt{3} \cong 1.155 \qquad (3.15)$$

The passband stems from the transmission line behaviour of the meandered line at higher frequencies. The shunt capacitance acts as a low impedance connection to ground at high frequencies. As a result, as frequency increases, the meandered lines act as quarter-wave short-circuit stubs and then as half-wave short-circuit stubs, etc.; the cell can thus be represented by the stub illustrated in Figure 3.3 (b). With the former, the RF short circuit is transformed into an open circuit. This allows transmission through the filter's microstrip line without impediment, giving rise to the upper passband seen in Figure 3.4, which lies inside the forbidden band of the EBG structure. With the latter, the RF short circuit is transformed back into a short circuit, stopping transmission through the filter's microstrip line, corresponding to the upper frequency roll off of the passband beyond the forbidden band in Figure 3.4. Further harmonic passbands and stopbands will also be evident, due to the three quarter-wavelength stub and full-wavelength stub, etc.
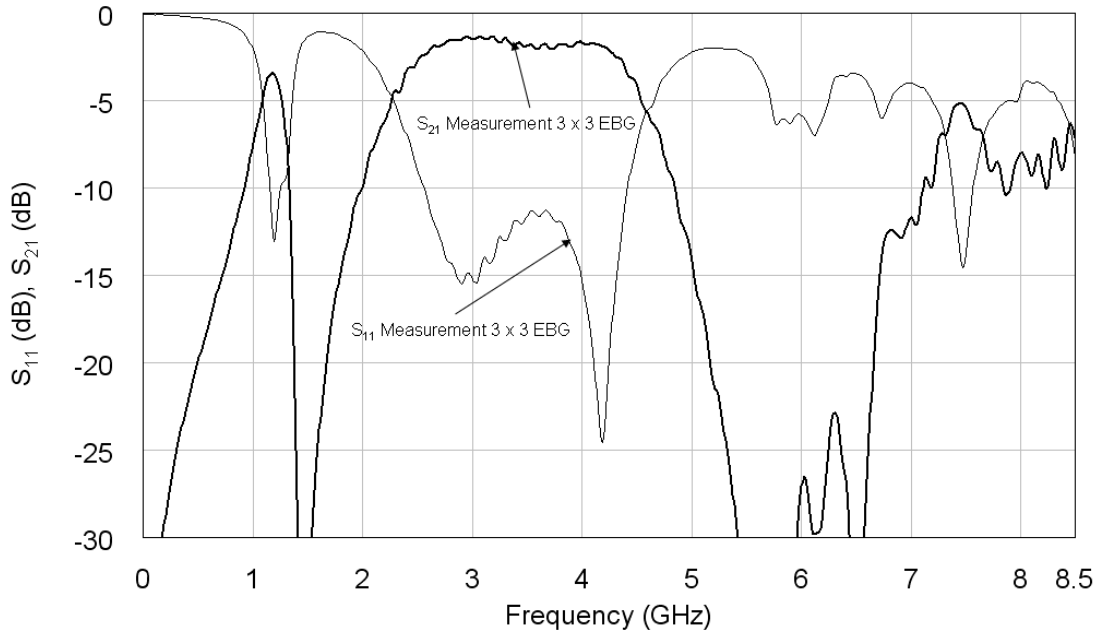
Figure 3.4 Measurement results for the 3 x 3 array EBG filter.

Therefore, the centre frequency of the band gap, which coincides with the passband of the filter implementation from Figure 3.4, depends on the length of the meander, which acts as a transmission line. Since the location of the transmission zero depends on the values of L_s and C_p (see (3.13)), the bandwidth can be influenced by changing the geometry of those components.

3.1.3 Dispersion Diagram

Because of the nature of the modified UC-EBG cell presented in this thesis, it is difficult to isolate one particular mode. For instance, with the 2nd mode, neither the electric nor magnetic field vectors are transversal to the propagation of direction.

Figure 3.5 shows the dispersion diagram for the PCB's modified UC-EBG cell with a periodicity of 10 mm, constructed using data points extracted from HFSS™.

45
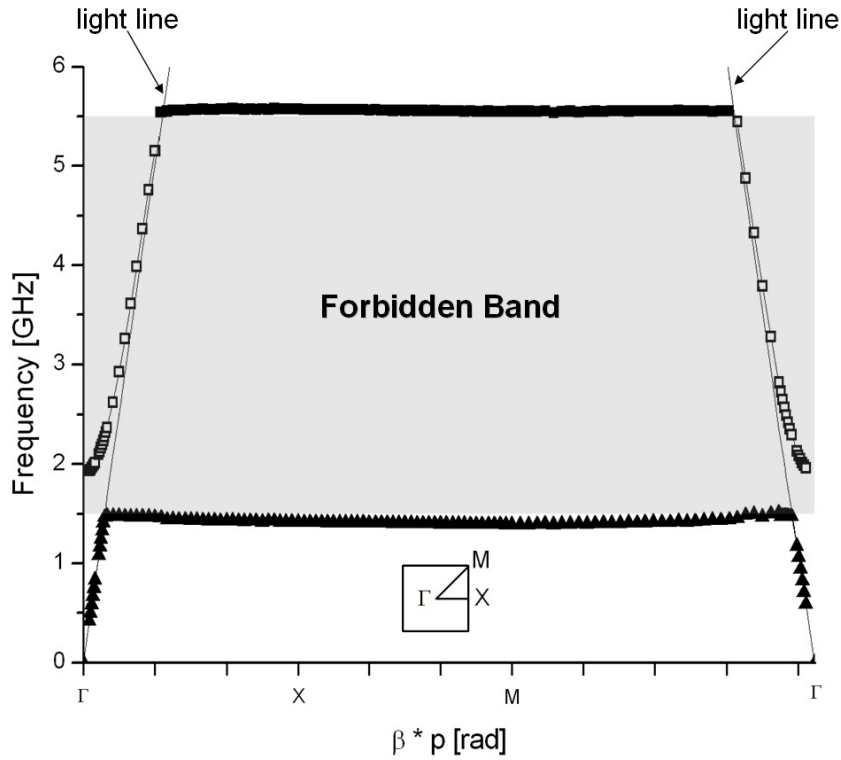
Figure 3.5 Dispersion diagram of the PCB modified UC-EBG cell with periodicity of 10 mm, determined with HFSS™.

Figure 3.5 shows the 1st and 3rd modes, which have been identified as being transverse magnetic (TM) in nature, from which the corresponding bandgap can be seen.

The solid points in Figure 3.5 have an unloaded quality (Qu)-factor > 59, with the exception of the point at 45° in the *M* to *Γ* branch, which has a Qu = 5.4. The hollow points have a Qu < 5.

For this reason, in Figure 3.5, the grey area in between the two TM modes denotes the forbidden band, which lies between 1.5 GHz and 5.5 GHz.

3.2 Monolithic Implementation

In order to further scale down the modified UC-EBG cell, a different fabrication method had to be used. Instead of PCB, a monolithic version was micromachined on fused silica wafers.

Figure 3.6 (a) shows a scanning electron microscope (SEM) micrograph of the monolithic implementation of the modified UC-EBG cell of periodicity 1 mm.

At the end of each meander, at the border to the adjacent cell, there is an anchor point. It can be seen in the side view (not to scale) of the monolithic version, shown in Figure 3.6 (b) that the cell is suspended above the wafer. The anchor points are attached to the substrate and provide the only mechanical supports for the cell. With the cells suspended above the substrate, a biasing pad could be designed underneath the cell. By applying a bias voltage between the cell and the pad, each cell would be an independent RF micro-electro-mechanical systems (MEMS) tuneable shunt capacitance. The meandered inductance lines would then also act as mechanical springs.
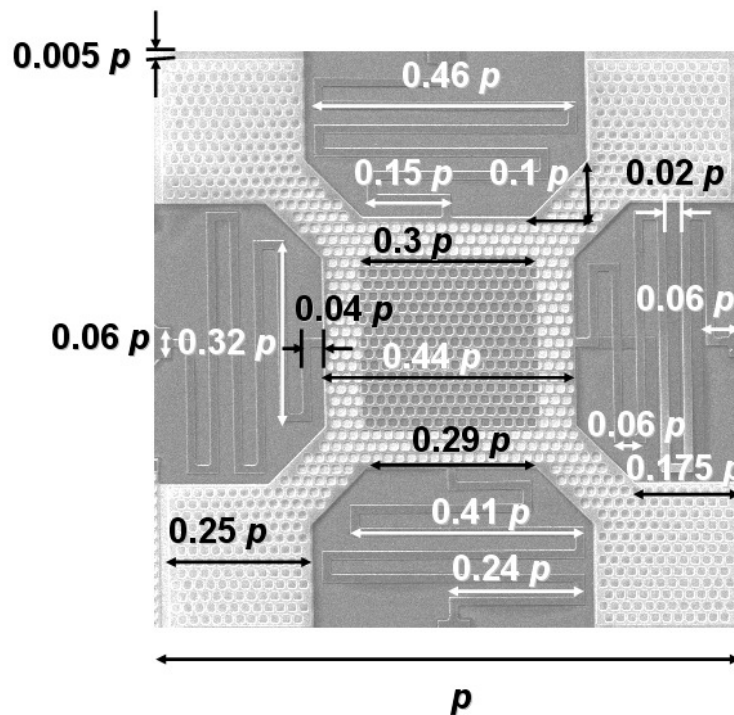
(a)
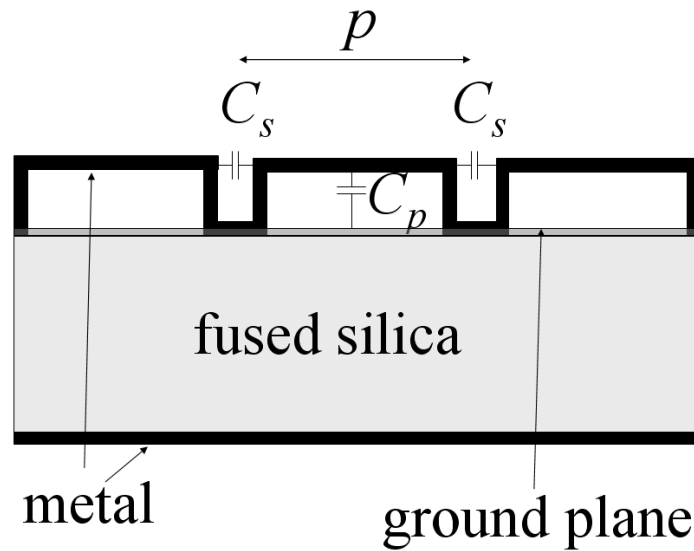
(b)

Figure 3.6 (a) SEM image of the modified UC-EBG cell with a periodicity of 1 mm on a fused silica substrate, including dimensioning. (b) side view of the modified UC-EBG cell on a fused silica substrate (not to scale).

3.3 Summary

Based on the UC-EBG cell, a modified UC-EBG cell is introduced. The inductances and capacitances of the modified UC-EBG cell are derived and their influence on the band gap is shown.

The dispersion diagram of the modified UC-EBG was numerically determined with HFSS™ eigenmode solver.

4 Printed Circuit Board Electromagnetic Bandgap Filters

With the cells desinged in chapter 3, a new way to construct a filter with EBGs is investigated. Typically, the EBG structure would be patterned on the ground plane, with the transmission line above it on top of the substrate [22]-[27]. A different approach employs the EBG in the same plane as the transmission line, leaving the ground plane unchanged. Since EBG structures prohibit the propagation of EM waves for a specific frequency band, the approach taken reverses that behaviour. Consider a microstrip transmission line. In order to introduce a band-pass filter behaviour, the line is surrounded by EBG structures on both sides. For frequencies where the EBG exhibits a bandgap, the EM waves travel along the transmission line, resulting in low insertion loss. Outside of the bandgap, the wave propagation through the EBG arrays is possible. Since the EBG array is connected to the ground plane, wave propagation along the transmission line will be highly attenuated. Thus, the filter effect of the EBG is reversed, since bandgap regions of the EBG become passbands for the signal along the line and vice versa. The generic layout of the EBG filter is illustrated in Figure 4.1. It consists of a central through transmission line with two symmetrical 2D EBG X x Y arrays on either side. At the periphery of each array, the cells are coupled to either the transmission line or ground strip via the cell's series inductance. It will be shown in Chapter 6 that a single defective cell can be introduced to provide tuneability to the filter. The term "defective" alludes to the introduction of defects in electron band gap materials. Thus, in this context, "defective" signifies an altered EBG cell.
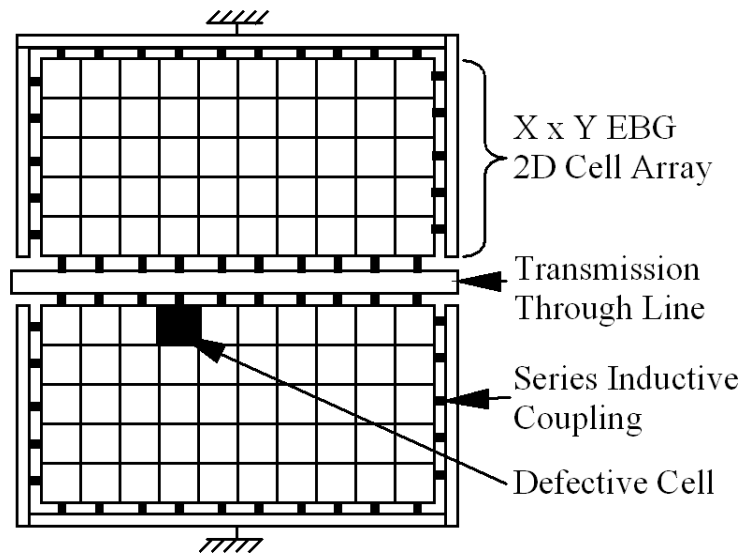
Figure 4.1 Generic layout of the UC-EBG cell array filter [40].

4.1 Approach

Designing and implementing a filter is a well understood process when quarter wavelength stubs or discrete components are used. The novel approach investigated within the thesis is to employ EBG structures to achieve a band-pass filter effect.

The following procedure describes the steps from design to device. Depending on the outcome of step 5, the process flow may loop back to step 2:

1. construct an equivalent circuit model to assist with the design of EBG filters and to predict their response.

2. design PCB EBG filter

3. predict the filter behaviour with 3D full wave simulations

4. fabricate and measure PCB EBG filter

5. verify the match of simulations and measurements

4.2 Equivalent Circuit Model

The behaviour of the filter was modelled with discrete components in microwave office, a 2D EM simulation software package. Creating an equivalent circuit model is important for two reasons: Firstly, it provides additional information about the structure's response. A 3D model can show the distribution of the fields in addition to the scattering parameters, but it does not show the size or influence of individual components. Secondly, an equivalent circuit model that accurately describes the behaviour can be modified in order to simulate design changes and / or modifications. The solutions for 2D simulations are typically obtained faster than the solutions of 3D simulations. The preferred method for design changes is a modification of the 2D equivalent circuit model, followed by the full wave 3D simulation once the 2D model yields good results.

The construction of the equivalent circuit model was an iterative process in the sense that it started with components for the cells that were gradually modified and replaced until the model provided a reasonable fit with the measurement.

Figure 4.2 shows the schematic of the 3 x 3 design. Only one of the two 3 x 3 arrays is shown in the picture. The cells described above are sub circuits, shown as blocks in the figure. Once the model of the design produced results that fit the measurements, any other designs could be easily simulated by adding or subtracting sub circuits.
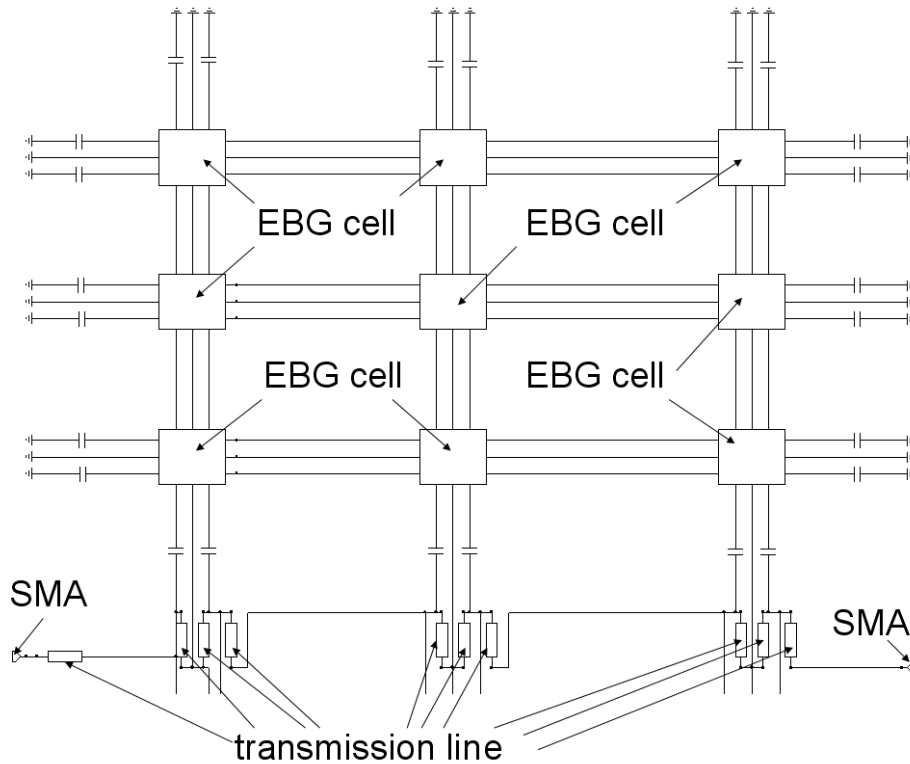
Figure 4.2 Schematic of the 2D array for the 3 x 3 EBG filter design.

Each of the EBG cells in Figure 4.2 contain the series capacitors. When two cells are connected, two of those capacitors are in series. To get the originally calculated capacitance value, the size of each of those capacitors has to be doubled, as 2 C_s in series with 2 C_s equals C_s. For the same reason, the edges of the EBG array in Figure 4.2 also contain capacitors.

Some of the designs directly connected the meanders of the cells together, in other designs the meanders ended in vias to ground. When vias were present in a design, the meanders of cells in the first row, which connects the main transmission line with cell, did not contain vias. For the example of the construction of the equivalent circuit model discussed here, the designs with vias were investigated.

The continuous transmission line was split up into transmission line segments in order to allow the meanders and capacitors to connect to the line in the appropriate places. The model of Figure 4.2 provided a good match at lower frequencies when the

EBG cells consisted of discrete components for L_s, C_s and C_p. However, it was not applicable at higher frequencies.

In chapter 3, the values of the components for a periodicity of 10 mm were calculated to be: C_s = 1.9 fF, C_p = 5.53 pF. The circuit simulator then extracted a value of C_p = 5.65 pF to give a better fit to measurements. At the second transmission zero, the extracted inductance value of the meander was found to be L_s = 7.15 nH, with each meander exhibiting an additional shunt capacitance to ground of $C_{p,meander}$ = 300 fF. This is also in good agreement with the calculated value L_s = 7.9051 nH.

The resonant frequency of the series inductor in parallel with both series capacitors is given by (4.1).

$$\omega_s = 1/\sqrt{2L_s C_s} \tag{4.1}$$

In order to provide a correct fit for the entire frequency range, the inductors had to be replaced with transmission lines in the equivalent circuit model.

4.3 Design

Due to the limitations of the network analyzer, a bandgap well below 8.5 GHz was selected. The modified UC-EBG cell analyzed in Chapter 3 was designed to exhibit a forbidden band between 1.5 GHz and 5.5 GHz at a periodicity of 10 mm. The PCB manufacturing process introduces additional limitations that have to be considered in the design process. Typically, FR4 is used for PCB application. However, FR4 has a worse dissipation factor of 0.01 at 1 GHz compared to other materials like Taconic RF35, which has a dissipation factor of 0.0018 at 1.9 GHz. Due to the lower loss tangent of RF35, it was chosen as a material for this application. For this test RF35 was obtained by Trackwise (a company specialising in PCB high frequency applications). Their minimum resolution for track width and gap width is stated as 25 μm [44]. Further

inquiries yielded guaranteed minimum track widths and gap widths of 200 μm with the preliminary design files [45]. Different filters with track widths and gap widths of 50 μm and 100 μm were investigated in addition to the modified UC-EBG with a track and gap width of 200 μm. Since EBGs can be scaled, it was expected that the bandgap would shift to higher frequencies with decreasing cell size, due to the increase of resonant frequency with decreasing capacitances and inductances (see (4.2)).

$$\omega_0 = \frac{1}{\sqrt{LC}} \tag{4.2}$$

The design itself is an iterative process – after the initial layout was sent, it was pointed out by trackwise that their process requires a metallic circle of at least 700 μm diameter around the via holes due to positioning tolerances [45]. This is a piece of information, which is not stated in the process specifications. Consequently, the design file had to be changed. The simulation file for the 3D Simulations was not changed. During simulations, the user usually makes assumptions to simplify a simulation model in order to cut simulation time, when an accurate depiction of the real device would not increase the accuracy of the simulation. Whether there is a circle around the vias should not influence their functionality. This assumption is proven by the excellent match between simulation and measurement, which can be seen in Figure 4.8.

4.4 Three Dimensional Full Wave Simulation

In order to predict the response of the EBG structures, Ansoft's HFSS™, a commercial 3D modelling package, was used. The simulation time of some of the structures presented in this work amounted to several days. It is clear that the results of predictive simulations need to be as accurate as possible within a reasonable time frame. As a method to reduce the simulation time, most of the simulations presented here employed the use of symmetry. HFSS™ documentation explains the use of symmetry boundaries

in great detail, but lacks descriptions about its accuracy. A simple comparison of setting up simulations of a transmission line connected to an EBG cell on each side, with and without a symmetry boundary, yielded the results shown in Figure 4.3:
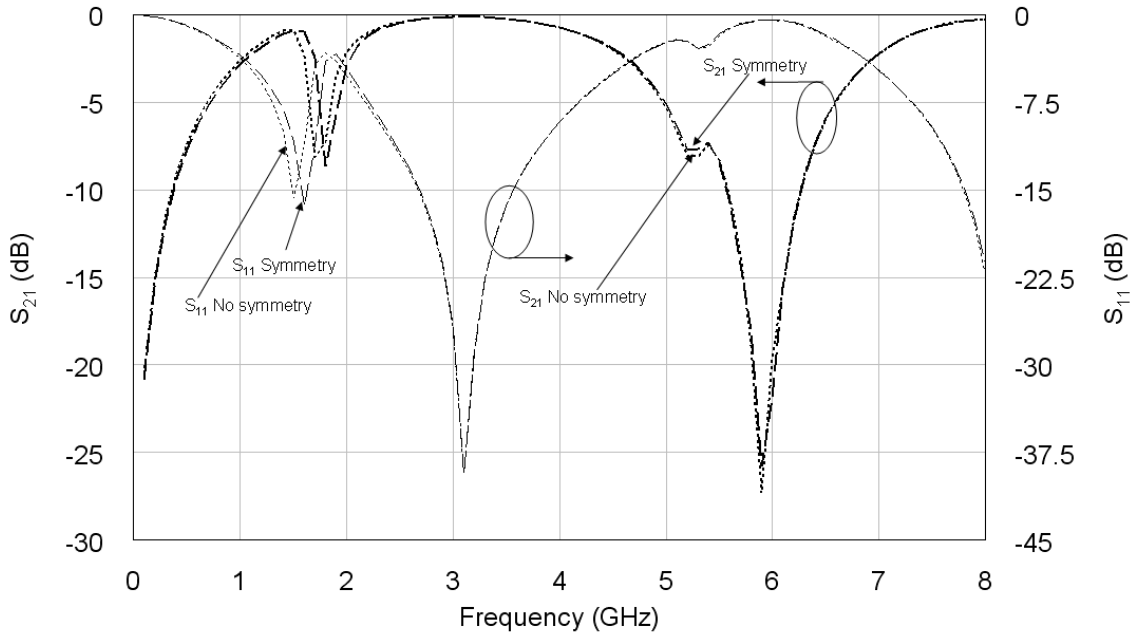
Figure 4.3 Comparison of simulation results with and without a symmetry boundary.

The thick lines are the insertion loss S_{21} and the thin lines represent the return loss S_{11}. The dashed lines are from the simulation with a symmetry boundary and the dotted lines belong to the simulation without symmetry.

It was found that the simulations have a maximum discrepancy of 7.5% below 2.5 GHz. At higher frequencies, both simulations were almost identical, even though there were a few frequencies with deviation as high as 5.5%. It should be noted that the comparison was done in dB, as the return loss and the insertion loss are typically plotted in dB. The discrepancies on a non-logarithmic scale could therefore be higher. Nevertheless, for the relevant frequency ranges in this work, it is sufficiently accurate to model structures with symmetry boundaries, effectively halving simulation times. More

55

important than the discrepancy in values is the frequency shift of 0.1 GHz at the resonances between the two simulations, which can be observed at lower frequencies.

For the promising PCB EBG Filters with a track width of 200 μm, HFSS™ was used to predict their behaviour. All of the following simulations were verified by the corresponding measurements, which are shown in the next section. Figure 4.4 compares the responses of the 4 x 1 and 4 x 4 filters. The thick lines are the insertion loss S_{21} and the thin lines represent the return loss S_{11}. The dashed lines belong to the 4 x 4 and the dotted lines to the 4 x 1 filter. Apart from the frequency shift at the resonance, both filters have an almost identical filter response. Since the meandered inductors between cells are shorted to ground, the inductive coupling between cells is negligible. Likewise, the capacitive coupling is around 1.9 fF per capacitor. As such, the capacitive coupling between cells can also be neglected. With neither significant capacitive nor inductive coupling between cells, the influence of rows beyond the first row of cells is greatly reduced, which explains why there is almost no difference between the 4 x 1 and 4 x 4 version of the filter. The frequency shift at lower frequencies is an artefact due to broader anchor points in the 4 x 1 simulation file. The width of the anchor points effectively shortens the meanders, as the anchors are vias to ground. Shorter meanders result in lower inductance, which in turn causes the frequency of resonance to increase.
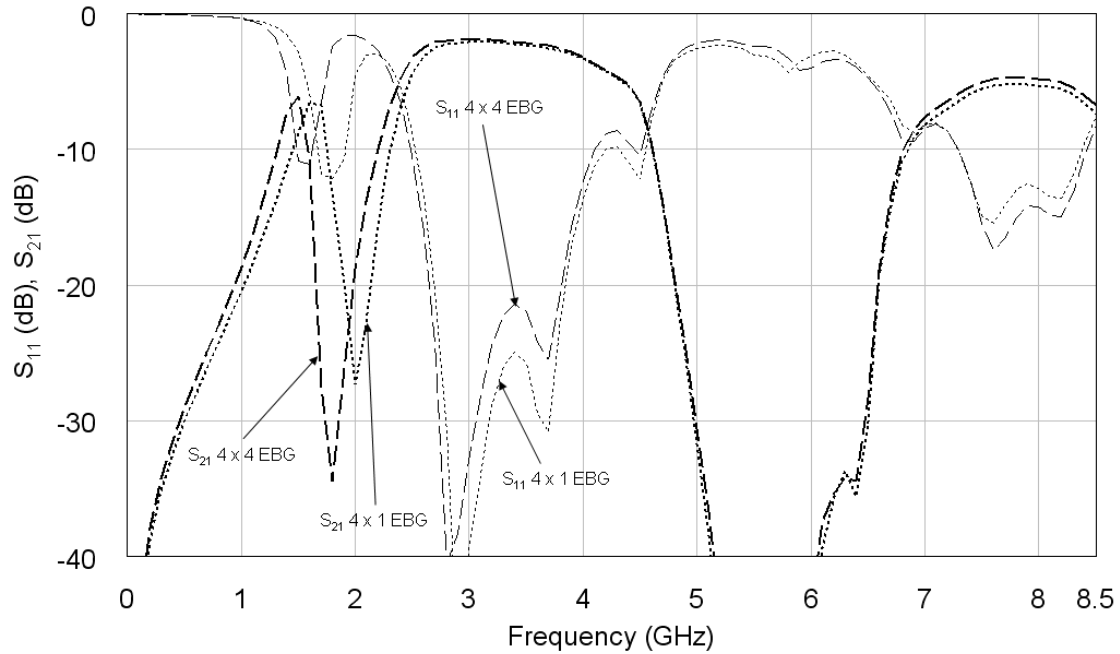
Figure 4.4 Comparison of simulation results of the 4 x 1 and 4 x 4 EBG filter.

With the main upper passband only, a very crude attempt was made to compare the effective equivalent filter order with that of a theoretical Butterworth filter approximation. Figure 4.5 shows the calculated insertion losses for three Butterworth band-pass filter approximations. From these, the 9th-order filter has the best fit. Even though the lower frequency roll-off characteristic is sharper with the calculated Butterworth approximation, the upper frequency roll-off is almost identical to that for the simulated 3 x 3 EBG filter.
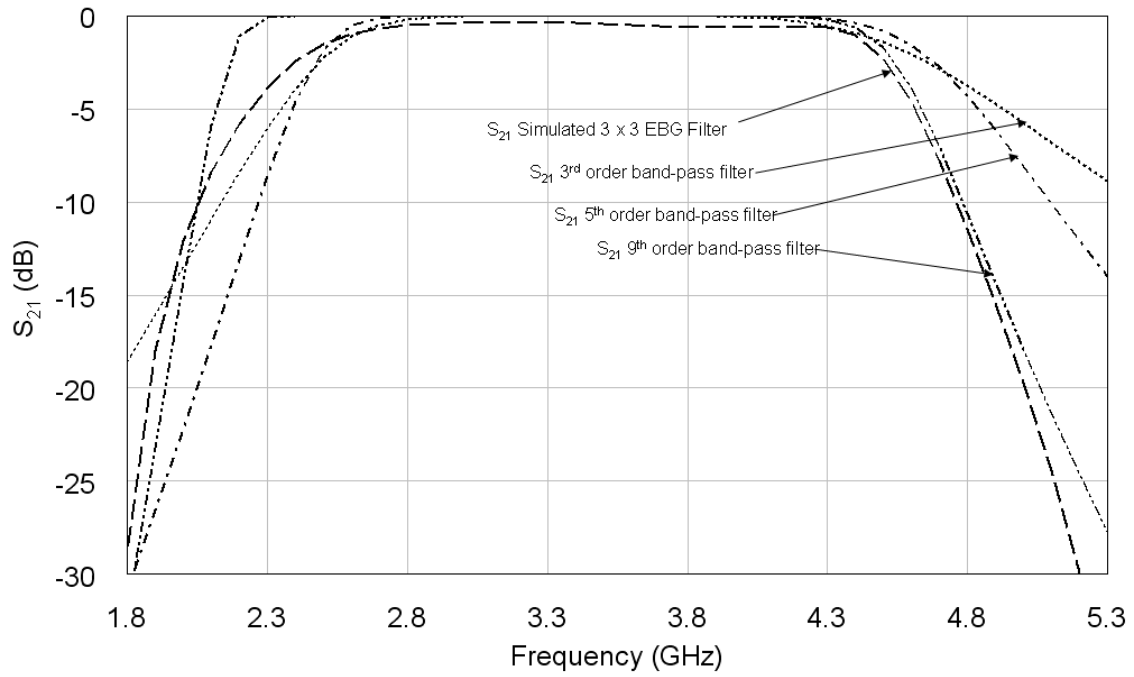
Figure 4.5 Estimation of the effective equivalent filter order.

The dashed line corresponds to the simulated EBG filter, the dotted line is a 3rd-order filter, the dashed-dotted line is a 5th-order filter and the dashed-double-dotted line is a 9th-order filter.

4.5 Fabrication

As mentioned in section 3.2 several EBG filters with different cell and array sizes were fabricated and measured. Figure 4.6 shows the PCB sheet with the various EBG filter designs.
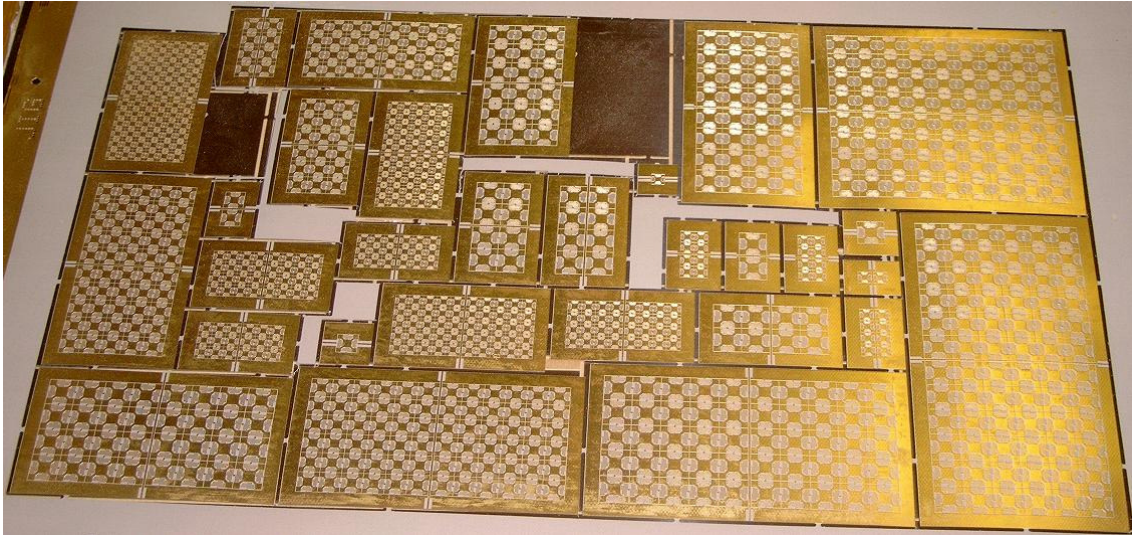
Figure 4.6 PCB sheet of the EBG filter designs.

Because the designs with a track width below 200 μm were not guaranteed by the manufacturer and because smaller feature sizes would shift the bandgap towards higher frequencies, which would exceed the range of the network analyzer, the thesis focuses on the 200 μm designs.

A close up of the 3 x 3 EBG filter with subminiature version A (SMA) connectors soldered onto it, can be seen in Figure 4.7.
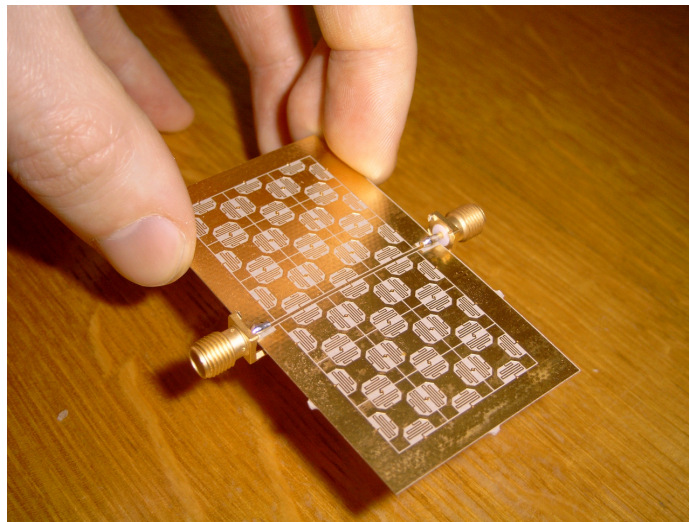
Figure 4.7 3 x 3 EBG filter with SMA connectors.

4.6 Match Between Simulations and Measurements

The predicted results for the scattering parameters are in good agreement with the measurement. The dashed lines in Figure 4.8 denote the HFSS™ simulation results. The thick line is the insertion loss S_{21} and the thin line is the return loss S_{11}.
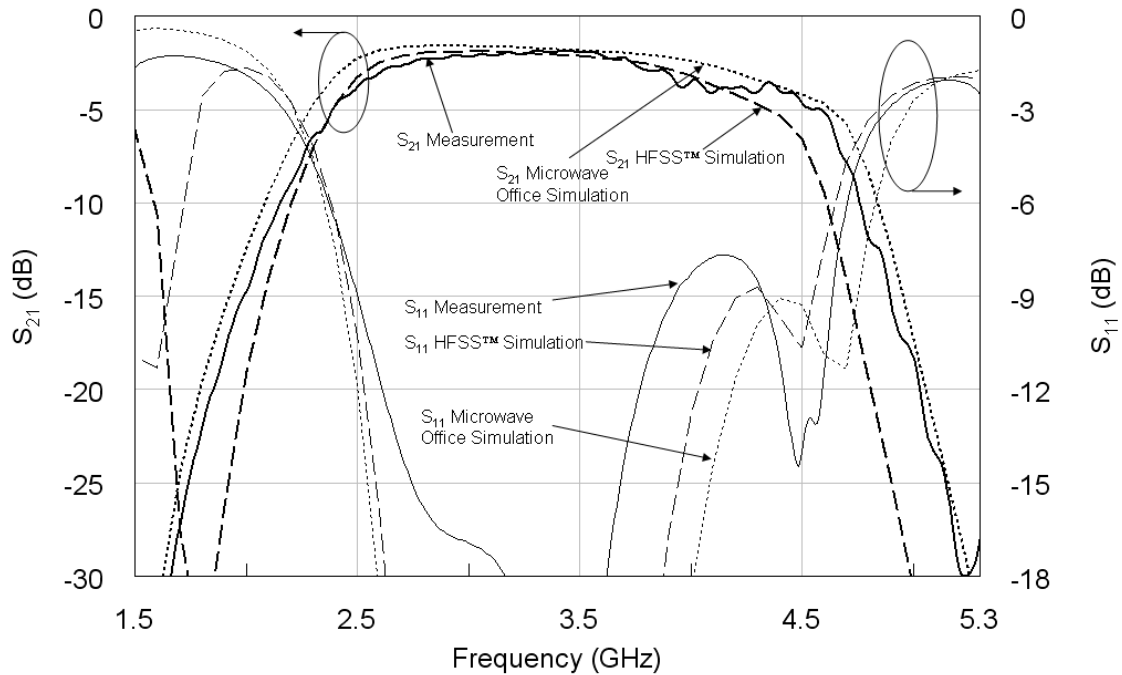
Figure 4.8 Measured and predicted performances for the 3 x 3 PCB EBG Filter.

In addition to the 3D model, the structure was also modelled with Microwave Office, a 2D simulator. The 2D model of the 4 x 1 filter array was based on a 3 x 1 model, which was devised for the aforementioned previous publication [16]. It was very easy to modify the 2D simulation by increasing the amount of EBG cells in the model, in order to accurately predict the response of the filter. This confirmed the versatility and accuracy of the 2D simulation. The results of the simulation are shown in Figure 4.8 as well. The thick dotted line is S_{21} and the thin dotted line is S_{11} of the Microwave Office simulation. The 2D Microwave Office simulation results are in good agreement with the measurement.

4.7 Summary

This chapter described the application of the modified UC-EBG cell, which was characterised in Chapter 3. The cell was used for the design of EBG filter arrays, which utilize the EBG structures in the same plane as the transmission line, opposed to the standard approach of using an EBG patterned ground plane to implement a filter. Several EBG filters with varying array and cell sizes were produced. Full wave simulations of the filters were in good agreement with the measurements. The structures were described by a 2D equivalent circuit model, which enables faster analysis of similar structures compared to full wave simulations.

5 Fused Silica Wafer Electromagnetic Bandgap Structure

In order to shift the passband to a higher frequency, the L- and C-components need to be decreased in size. This is achieved by reducing the feature sizes. The limitations inherent to PCB technology prevents further size reductions. Micromachining an EBG filter on a chip provided the solution to overcome the minimum widths associated with PCB etching. The additional benefit of micromachining the EBG structure on wafers is the compatibility with commercial fabrication processes.

Two foundries from the Advanced MEMS for RF and Millimeter Wave Communications (AMICOM) network of excellence were chosen for the fabrication of the chip EBG filter. One was ITC-irst in Italy and the other was VTT MililLab in Finland. Both had similar design constraints with the track width and gap width set at 10 µm for their multi project wafer (MPW) run.

5.1 Design

Apart from minor corrections, the shape of the cell was retained while the cell size was reduced from 1 cm^2 to 1 mm^2. Scalability would suggest that the centre frequency has been increased by a factor of 10. This would put the centre frequency at 35 GHz. However, the substrate material has not been scaled. Where before RF35 was used, the substrate in the wafer design was fused silica. Since the EBG array is suspended above the wafer, the relevant substrate material is air.

Figure 5.1 (a) shows the seven lithography mask layers of the design. Figure 5.1 (b) is a close up of the EBG cell. It can be seen that the bridge layer, which is the green

area in Figure 5.1 (b), contains holes. These holes are required for the fabrication process: The bridge layer is deposited on a sacrificial layer. After the removal of the sacrificial layer, the bridge layer forms free standing structures, for instance the suspended EBG cells. In order to remove the sacrificial layer, solvent needs to bypass the bridge layer, which is one purpose of the holes. According to [46], the perforation has a negligible effect on the up-state capacitance. Including a perforation also has the benefits of reducing the Young's modulus of the structure and of lowering the structure's mass [46].

(a)   (b)
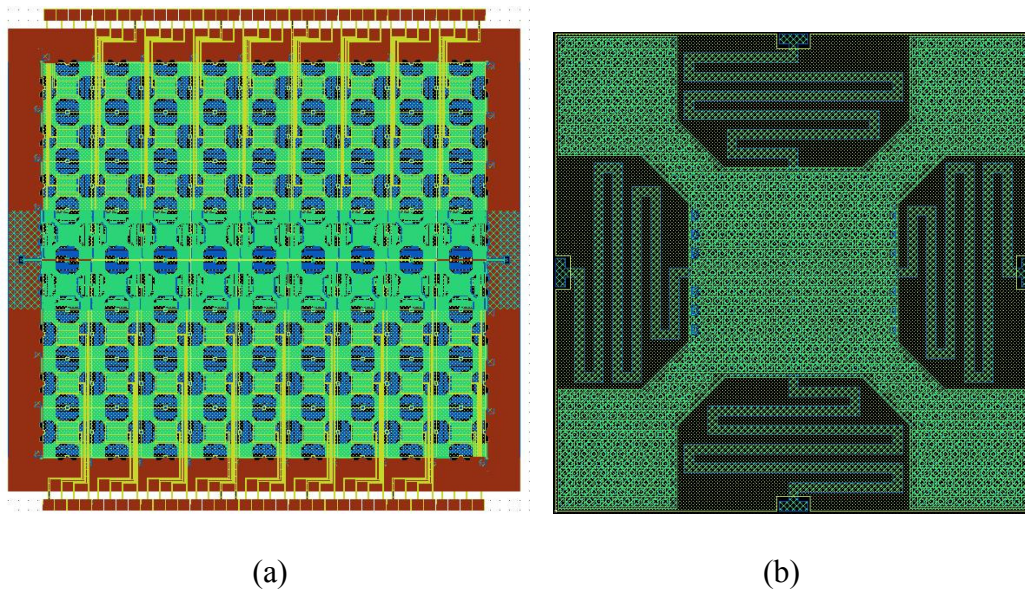
Figure 5.1 (a) Top view of the lithography mask layers of the design, (b) top view of the modified UC-EBG cell.

The holes for the ITC-IRST multiproject wafer run had to be circular, whereas the holes for the VTT MilliLab wafer run had to be rectangular. This illustrates that despite a similarity in the process flow and in the design itself, certain changes had to be made according to other people's specifications.

The VTT MilliLab multiproject wafer run provided twice as much space as the ITC-irst run. In addtion to the $1 \times 1 \text{ cm}^2$ filter design, a $1 \times 1 \text{ cm}^2$ EBG array for use as a reflect array, was included in the VTT MilliLab run.

63

Figure 5.2 shows the simulation and comparison of different ground plane configurations. It can be seen that the configuration with a continuous ground plane, which is similar to the set up of the PCB EBG filter, does not produce useful results. When the ground plane underneath the meanders is removed, the meanders mainly function as inductors, instead of exhibiting shunt capacitance. With this octagonal ground plane, the response of the structure is similar to the PCB version. The EBG arrays are hanging above the substrate in both designs. In a real world prototype, the EBG cells have to be connected to the substrate in some spots. The dotted line shows the EBG array with the octagonal ground plane and with the four anchor points of each cell connected to the substrate. It can be seen that the low frequency behaviour of the structure is highly attenuated.
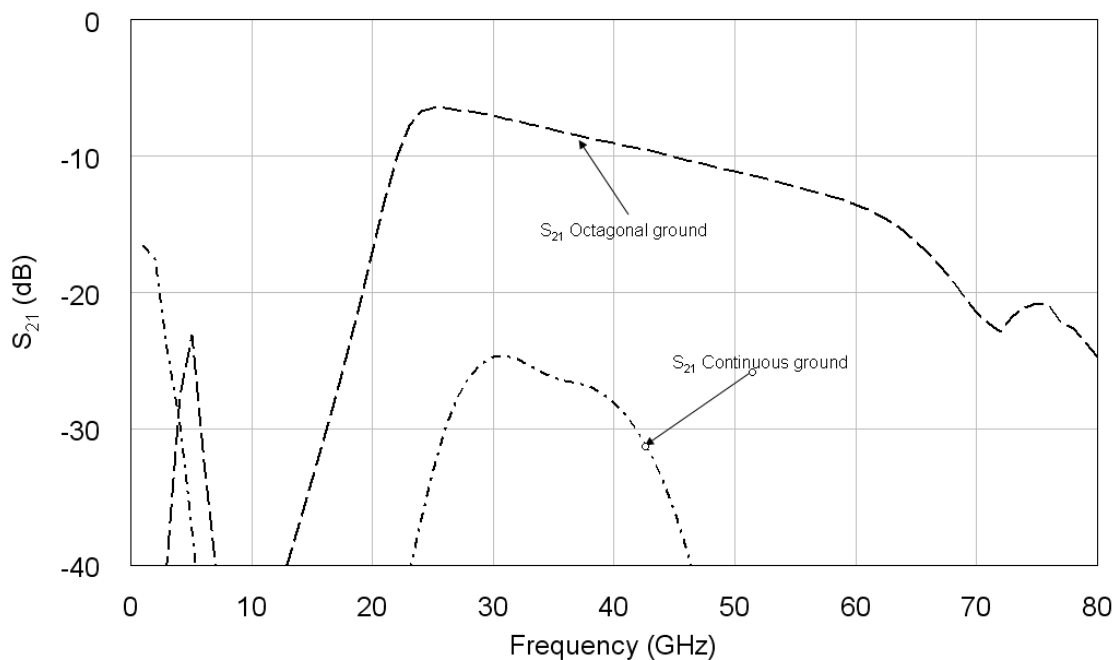
Figure 5.2 Comparison of continuous ground with the octagonal ground plane configuration for the monolithic EBG structure.

The shape of the octagonal ground plane is shown in Figure 5.3 for 2 x 2 cells. The area underneath the meanders creates the octagonal shape. The ground plane

underneath the main part of the cell is not continuous in order to leave room for a pad for electrostatic actuation.
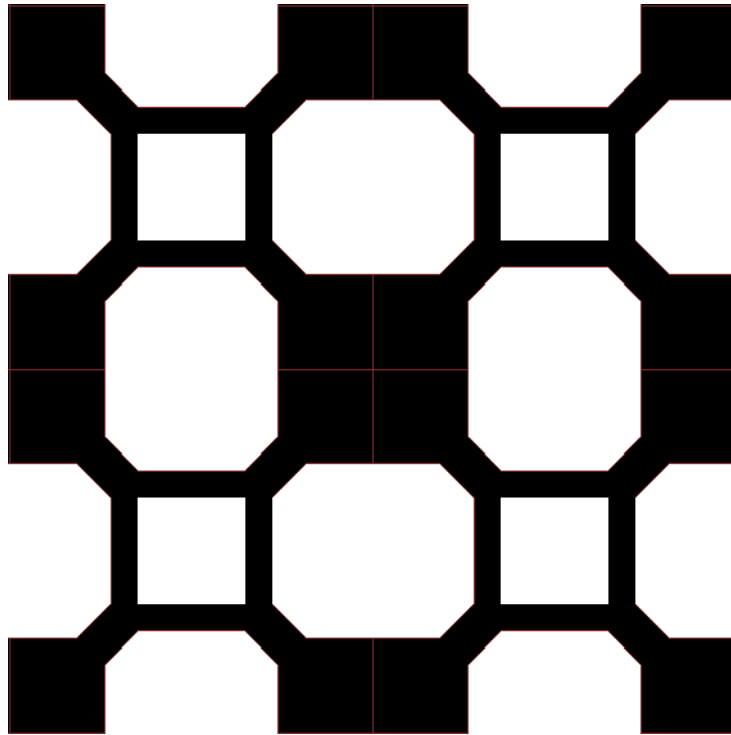
Figure 5.3 Octagonal groundplane for a 2 x 2 cell array.

The material parameters vary from process to process and the design rules only list rough values that could be used as a guideline, if they list anything at all. As such, predictive simulations tend to be overly optimistic. For instance, losses of the actual hardware are higher in comparison to a simulation with bulk conductivity values, due to the sheet resistance of thin films. The value of the sheet resistance and the corresponding conductivity of the material was determined in an iterative approach. Section 4.3 deals with the measurements and simulations, the derived material properties are listed there.

Figure 5.4 shows the attenuation and roll off at the passband for filters with one row and an increasing number of cells from 1 x 1 to 9 x 1. At nine cells, the passband has the steepest roll off characteristic.
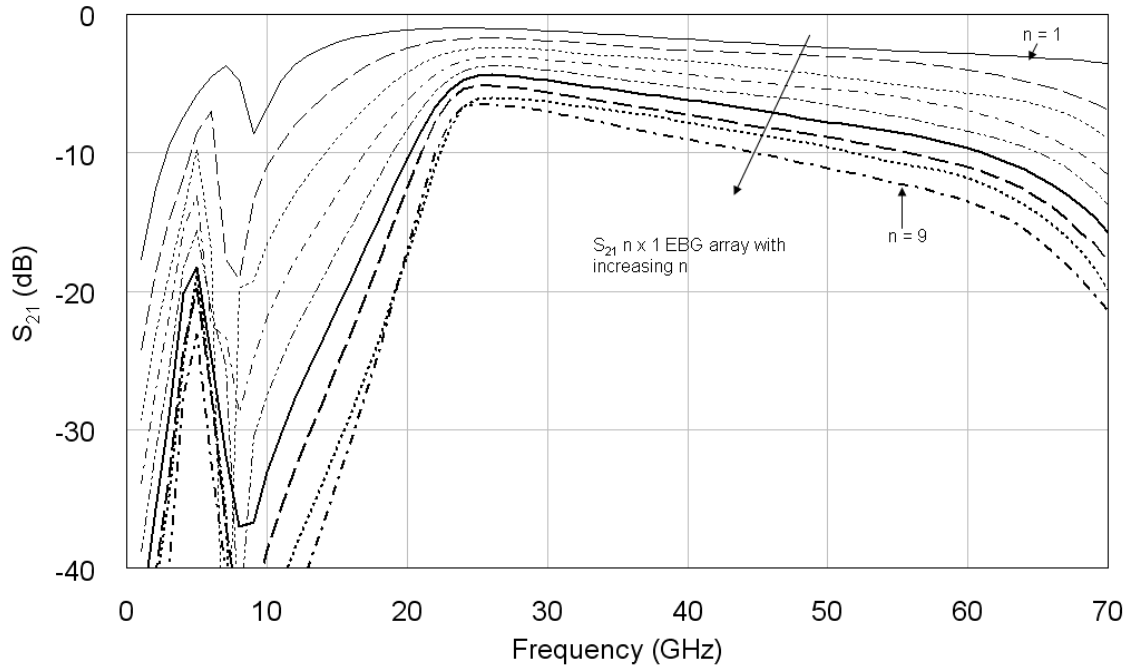
Figure 5.4 Monolithic EBG filter simulations with n x 1 cells.

Table 5.1 shows the insertion loss of the EBG filter arrays with 1 x 1 to 9 x 1 cells at 5 GHz, which is the position of the low frequency resonance, and at 25 GHz, the beginning of the passband region.

Table 5.1 Simulated Insertion Loss at 5 GHz and 25 GHz for Different

Numbers of Cells

Cells	S_{21} at 5 GHz (in dB)	S_{21} at 25 GHz (in dB)
1 x 1	-5.77	-1.00
2 x 1	-8.53	-1.70
3 x 1	-9.72	-2.43
4 x 1	-13.12	-3.13
5 x 1	-15.60	-3.81
6 x 1	-18.26	-4.44
7 x 1	-19.83	-5.14

Cells	S_{21} at 5 GHz (in dB)	S_{21} at 25 GHz (in dB)
8 x 1	-18.57	-6.13
9 x 1	-23.12	-6.47

At 25 GHz, the insertion loss decreases by roughly 0.7 dB per additional cell. The unwanted peak at the low frequency resonance is attenuated by significantly more than the 0.7 dB per cell. The difference in attenuation between the 25 GHz and 5 GHz point is less than 5 dB for one cell and more than 16.5 dB for a 9 x 1 array filter.

Figure 5.5 is a comparison between designs with nine cells, but with different numbers of rows. Unlike the PCB version, the EBG cells are electrically connected. It can be seen that additional rows of cells have an effect on the insertion loss. With an increasing number of rows, the attenuation generally rises. For instance, at 75 GHz, the attenuation is -20.78 dB for one row, -26.47 dB with two rows and -36.65 dB with four rows.
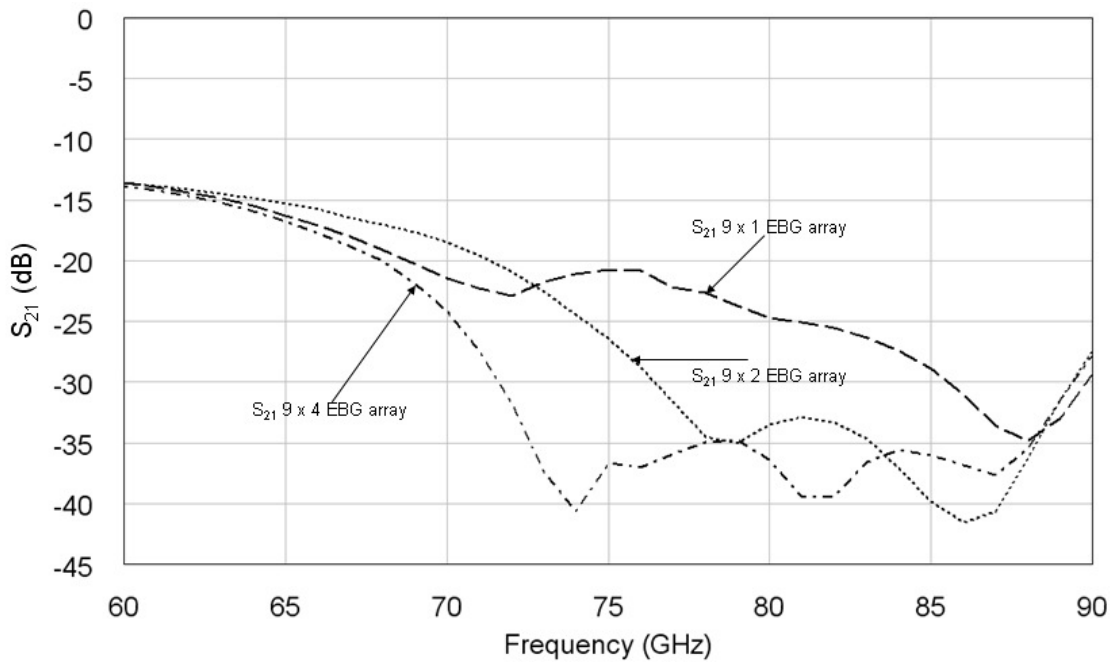
Figure 5.5 Monolithic EBG filter simulations with increasing numbers of rows.

The results shown in Figure 5.4 and Figure 5.5 are the reason for choosing to build a filter with EBG arrays of 9 x 4 cells on each side of the microstrip transmission line.

The tuning methods used in the PCB filter are impractical for the chip filter. The current version of the chip filter is not tuneable. All the structures are suspended in order to enable MEMS tuneability in a future iteration of the design.

The transmission line is made of the bridge layer in both designs. The bridge layer was 1.8 μm gold at ITC-irst and 1.5 μm aluminium at VTT MiliLab, with an air gap of 3 μm and 2.3 μm respectively. The line width of 18.5 μm was calculated with the program txline. Since the transmission line is suspended, it was attached to the substrate at anchor points, which were spaced out by 1 / 3 of a millimeter on average. The exact spacing between anchors was 300 μm, 400 μm and again 300 μm per 1000 μm cell.

5.2 Fabrication

Figure 5.6 shows SEM micrographs of different sections of the monolithic EBG structure built at ITC-irst. Figure 5.6 (a) displays almost the complete structure at the lowest magnification of the SEM. Figure 5.6 (b) shows two suspended meanders, which are connected with the substrate at one of the anchor points. In the middle of Figure 5.6 (c) the suspended microstrip transmission line with its anchor points can be seen. The first row of cells on each side of the transmission line is shown as well. Figure 5.6 (d) shows biasing lines and pads intended for electrostatic actuation of the cells. A production flaw can be seen on the grounded frame.
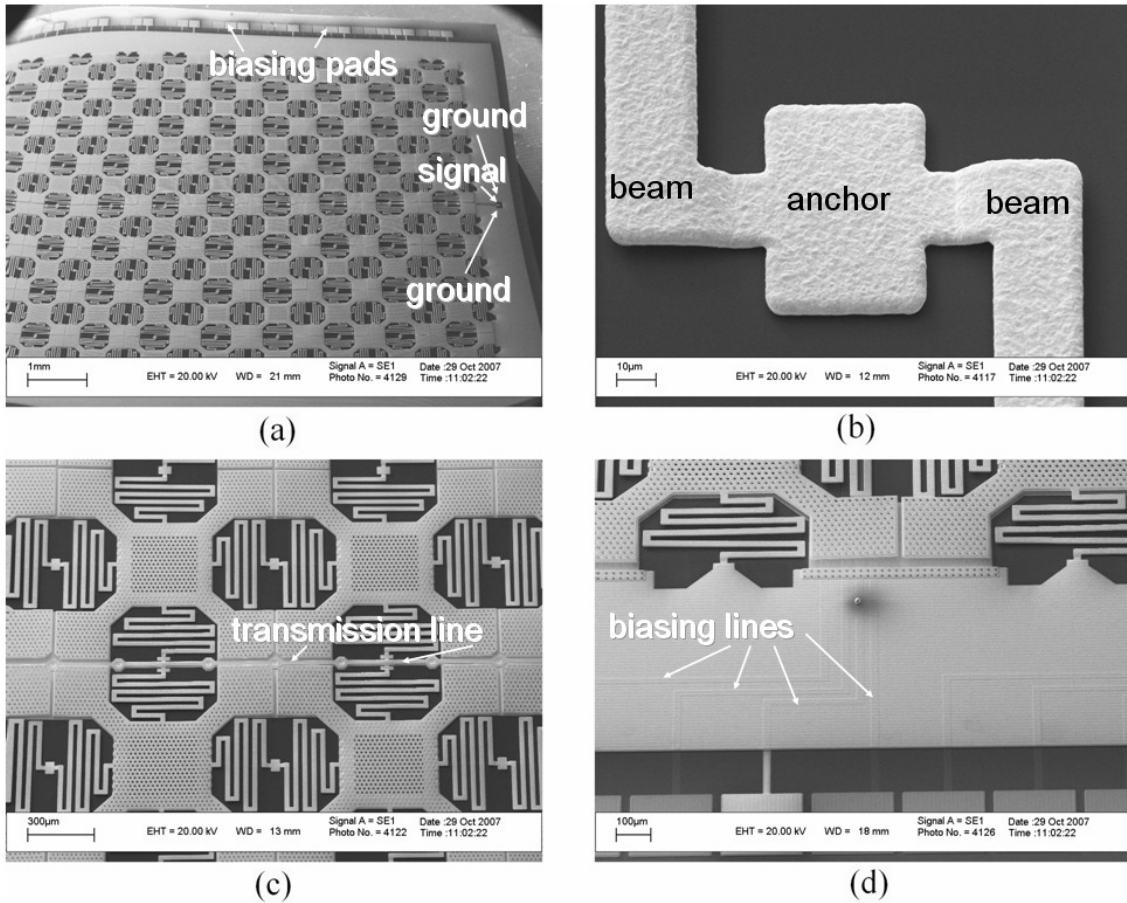
Figure 5.6 (a) View of the monolithic EBG structure fabricated by ITC-irst (b) meanders connected to an anchor point (c) suspended microstrip transmission line flanked by two EBG arrays (d) biasing lines and pads.

After the fabrication of the monolithic EBG structure, optical profilometer measurements were performed by ITC-irst. Figure 5.7 (a) shows the scanning path along the EBG cell. The colours indicate the displacement, starting with the highest in red to the lowest in blue.

Figure 5.7 (b) is a 3D view of the deformation. Figure 5.7 (c) shows the surface profile of the scanned EBG cell.
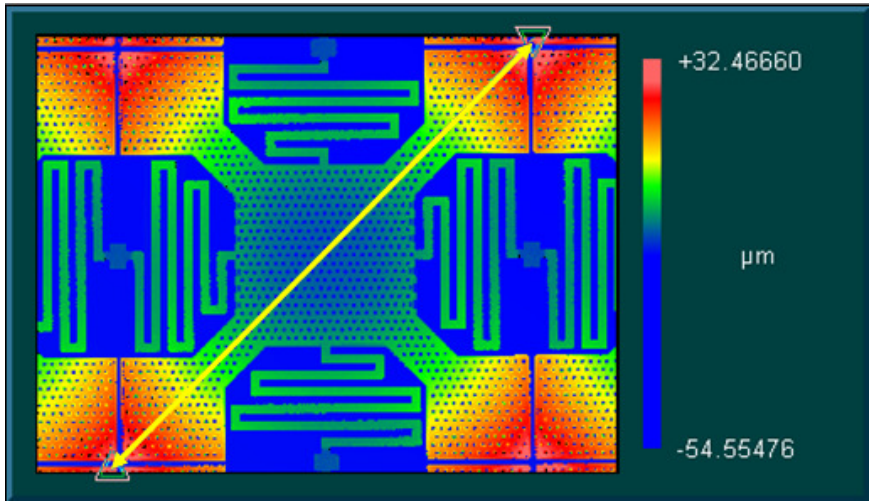
(a)
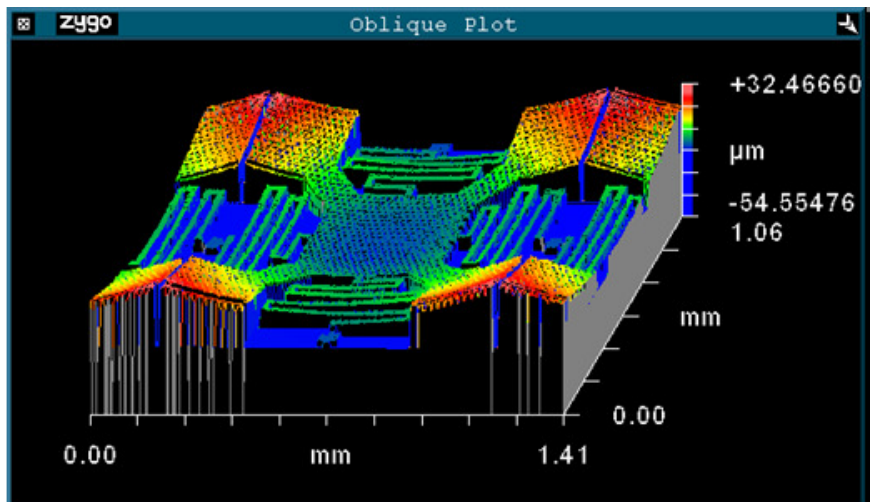
(b)
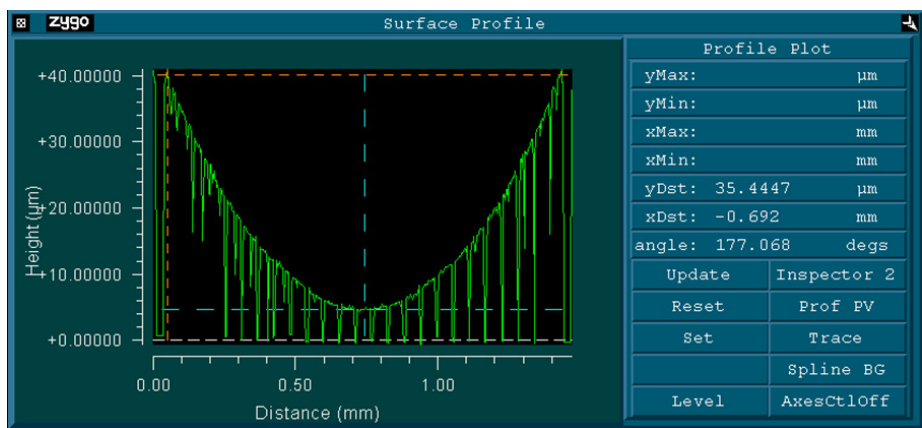
(c)

Figure 5.7 (a) Scanning path, (b) 3D view and (c) Surface profile of an optical profilometer measurement by ITC-irst.

These measurements show that the side capacitances are bent upwards by 35 μm. The resulting change in capacitance due to this deformation will only have an effect on the low frequency behaviour of the structure. A comparison of the simulation results with the measurements, both of which are shown in Figure 5.10, reveals that a simulation with assumed flatness is sufficiently accurate.

Figure 5.8 shows a cell of the monolithic EBG structure manufactured by VTT MilliLab. The micrographs of Figure 5.8 (a) and Figure 5.8 (b) were taken within a few seconds of each other. Due to the uniform build up of negative charge, the cell is repelled. In Figure 5.8 (b) it can be seen that the meanders are not breaking or snapping off at the anchor points, but are indeed acting as mechanical springs. During normal operation of a MEMS tuneable shunt capacitance, the displacement is restricted to the size of the bridge layer, which provided the distance between the suspended cells and the substrate. This distance is 2.3 μm for the VTT MilliLab design and 3 μm for the ITC-irst design. This means that during normal operation, the meanders will not be strained as severely as in the extreme case shown in Figure 5.8.

(a)   (b)
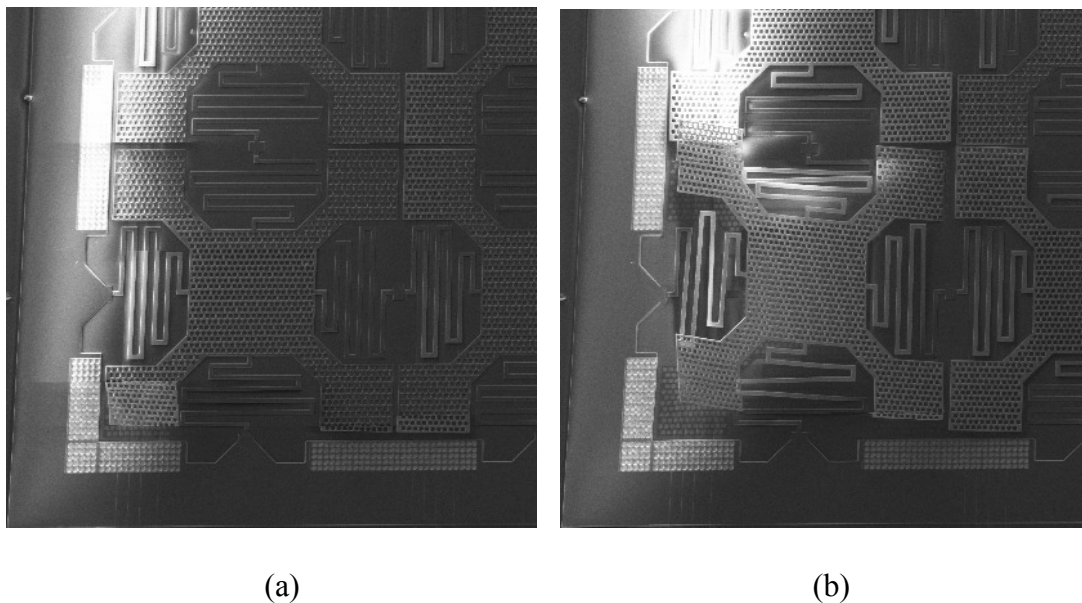
Figure 5.8 (a) EBG cell, (b) charged EBG cell is repelled by charged ground plane.

5.3 Measurement

This section discusses the measurements of the first monolithic prototype that was fabricated by VTT MiliLab. The bridge layer, which gives suspended structures, is made of 1.5 μm sputtered aluminium. The multi-metal (i.e. 50 nm TiW, 400 nm Au and 50 nm TiW) ground plane was approximated by a 500 nm gold layer within the HFSS™ simulations. Since bulk conductivity cannot be applied to thin films, approximately one third of the conductivity (1.2×10^7 S / m for the aluminium and 1.3×10^7 S / m for the gold layer) was assumed for these simulations, to account for the higher sheet resistance of the thin films.

Figure 5.9 shows the complete filter on the left-hand side and a magnification of the through transmission line on the right-hand side, with adjacent cells above and below this line. The complete area of the filter is only 1 cm^2, with the dimensions of each cell being 1 x 1 mm^2. Similar to the PCB filter, two modified UC-EBG cell arrays are connected to a central microstrip through transmission line. The size of the array has been expanded to 9 x 4 cells. Unlike the PCB version, the microstrip line and the EBG cells are suspended 2.3 μm above the wafer and connected to the fused silica substrate with electrically-isolated anchors.
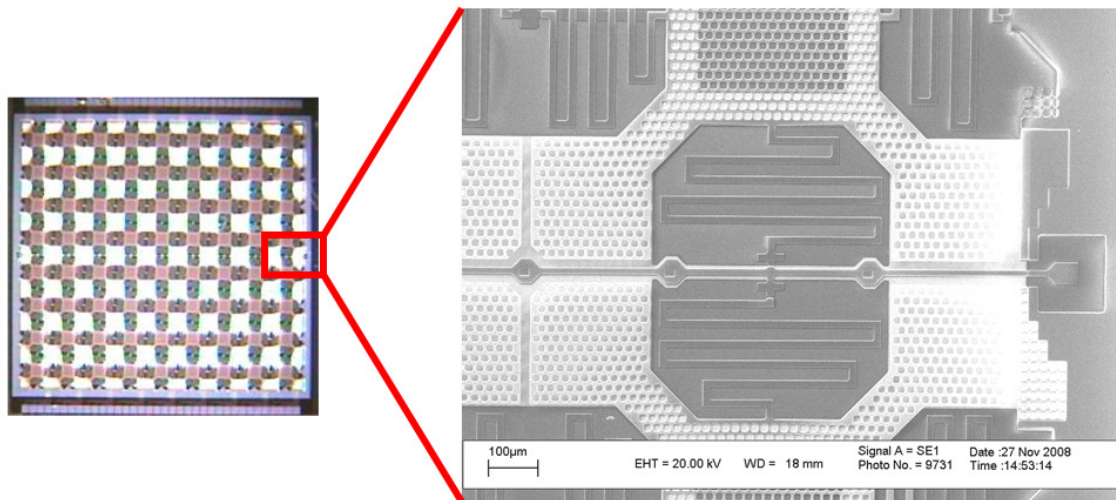
Figure 5.9 Magnified photograph of the fused silica wafer EBG structure and magnified SEM micrograph of the probe pad and transmission line.

Figure 5.10 shows the insertion loss and return loss of both the predicted HFSS™ simulations (dotted line) and measurement (solid line) of this new filter. It can be seen that the measured performance is in good agreement with that predicted. Also shown in Figure 5.10, the predicted insertion loss performance (dashed line) of the suspended microstrip line is given, having the same material properties and dimensions as that for the filter. It can be clearly seen that the slope within the passband of the filter is bounded by the insertion loss of the discrete transmission line.

Therefore, it can be deduced that the transmission line losses need to be reduced further, in order to be able to realize a more characteristic band-pass filter response.
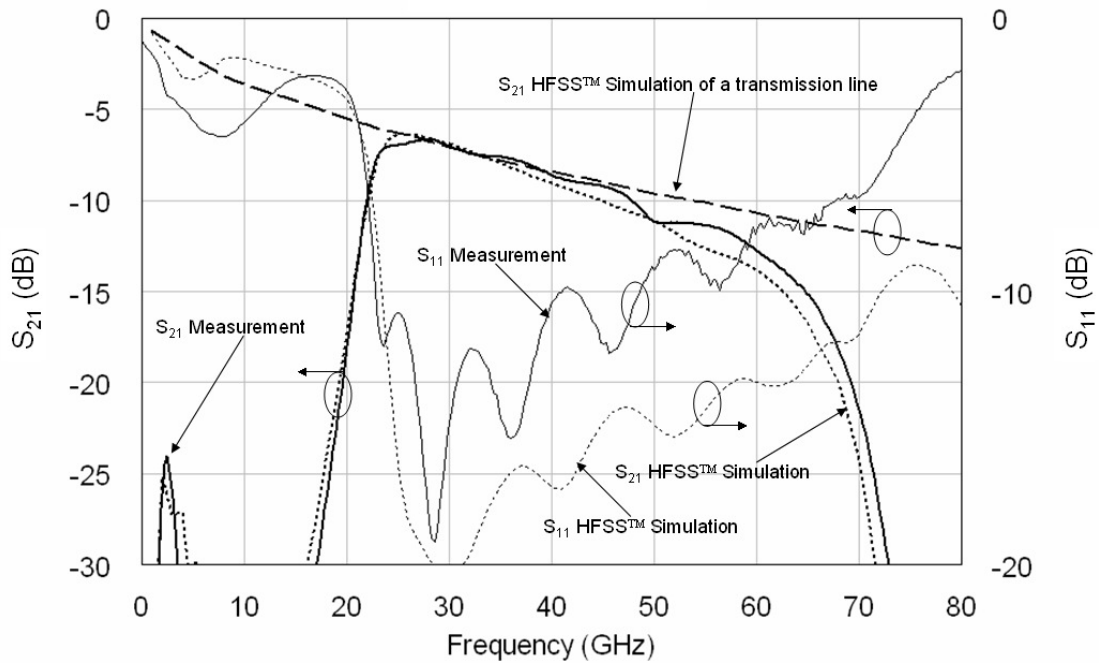
Figure 5.10 Simulation and measurement results of the monolithic EBG structure.

5.4 Summary

The modified UC-EBG cells were scaled down by a factor of 10 in order to shift the band to higher frequencies. The monolithic EBG structures were fabricated externally with a fabrication process compatible with commercial foundries.

The simulation results are in good agreement with the measurements, however the slope of the passband is bounded by the slope of the transmission line, which suggests that the transmission line losses need to be decreased in order to attain a better filter characteristic.

6 Tuneability

In order to improve the functionality of EBG and metamaterial structures, their properties can be made tuneable. Typically, the tuning approach consists of changing the inductive or capacitive properties of the structure and, thus, the frequency of resonance for individual cells. Several methods for tuning EBGs and metamaterials have been proposed in the literature; for example, capacitive elements are tuned by exploiting the temperature dependence of the associated dielectric constant of ferroelectric thin films [47]. A large number of publications describe methods of tuning the capacitance by adding varactors [48]; this appears to be the most common method of tuning. For instance, ferroelectric varactors have been used to tune the behaviour of left-handed phase shifters [49]. Instead of tuning the capacitance, an equivalent approach is to use tuneable active inductors [50]. Moreover, a DNG was built with magnetodielectric spherical particles and their properties were tuned with a magnetic field of varying strength [51]. Switching between two states is another method of implementing tuneability, which was realized with MEMS switches on SRRs [52]. Optical control, i.e. illumination of semiconductors to generate electron-hole pair free carriers, has also been used to tune SRRs [53]. Alternatively, PIN diodes can also be used within a FSS, to control the operating frequency of an EBG resonator antenna [54]. Finally, liquid crystals have been employed to tune FSS [55].

6.1 Optical Tuneability

The first idea to introduce tuneability to the PCB EBG filter revolved around the excitation of carriers in semi conductors by illumination. Figure 6.1 shows the schematic of the principle. A piece of high resistive silicon (HRS) is positioned above

the transmission line and the EBG array of the filter. HRS was chosen in order to prevent a direct electrical connection between the transmission line and the EBG cells. The glass on top of the silicon is necessitated by the experimental setup: Since the HRS is not part of the filter, the air gap between the filter and the HRS needs to be removed or at least minimised. The HRS itself is too thin and brittle to withstand the pressure of the clamps. For this reason, a microscope slide was placed on top of the HRS, before clamps pressed the PCB, HRS and the glass slide together.
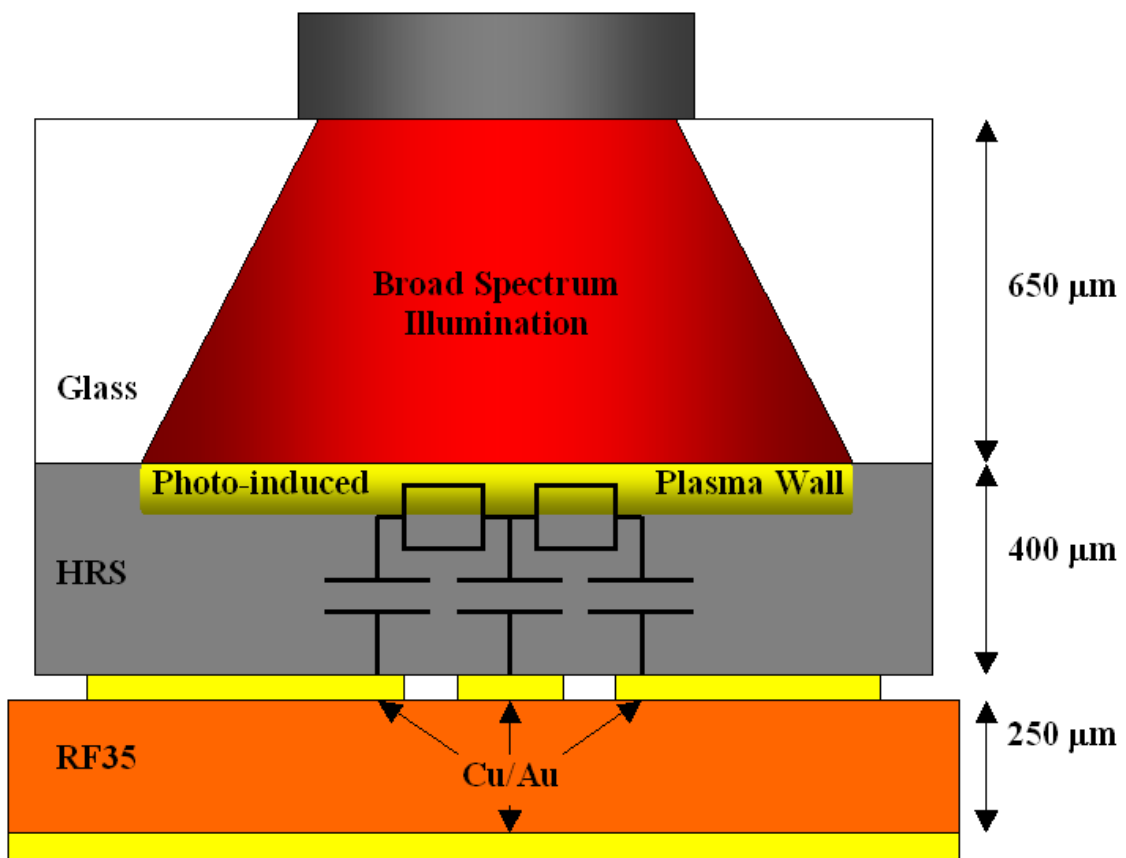
Figure 6.1 Schematic of the optical tuneability experiment.

In the experiment a 150 W halogen lamp served as light source. The broad spectrum illumination excites electron-hole pairs in the surface of the HRS. As such, the yellow layer in Figure 6.1 labelled photo-induced plasma wall can be considered to be a conductive surface. The schematic shows capacitances between this surface and the EBG arrays as well as the transmission line. Along the photo-induced plasma wall, the

resistance is lowered in comparison to the bulk HRS region due to the free carriers. Typically, switching between two states by lowering the resistance with optical illumination is the technique used in literature [56],[57]. The experimental set up can be seen in Figure 6.2.

Figure 6.2 Measurement set up of the optical tuneability experiment.

All the elements from the schematic are in the picture in addition to the network analyzer leads, the clamps and microscope slides underneath the PCB to provide grip for the clamps.

Figure 6.3 shows one measurement result for the 4 x 1 EBG filter. Three states have been measured and compared for the insertion loss S_{21}: The solid line denotes the filter response with no illumination. The dotted line stands for an illuminated state and the dotted-dashed line represents flood light, with the light source at maximum power. It can be seen that there is no shift in frequency between the three states. The only

noticeable effect is an increase of losses. Changing the position of the illumination away from the microstrip line and the first row of EBG cells to areas between EBG cells, which can be found on the 4 x 4 EBG filter, did not influence the behaviour of the filter. This is to be expected due to the vias to ground at the end of the meanders, which short out subsequent cells as mentioned in Chapter 3.
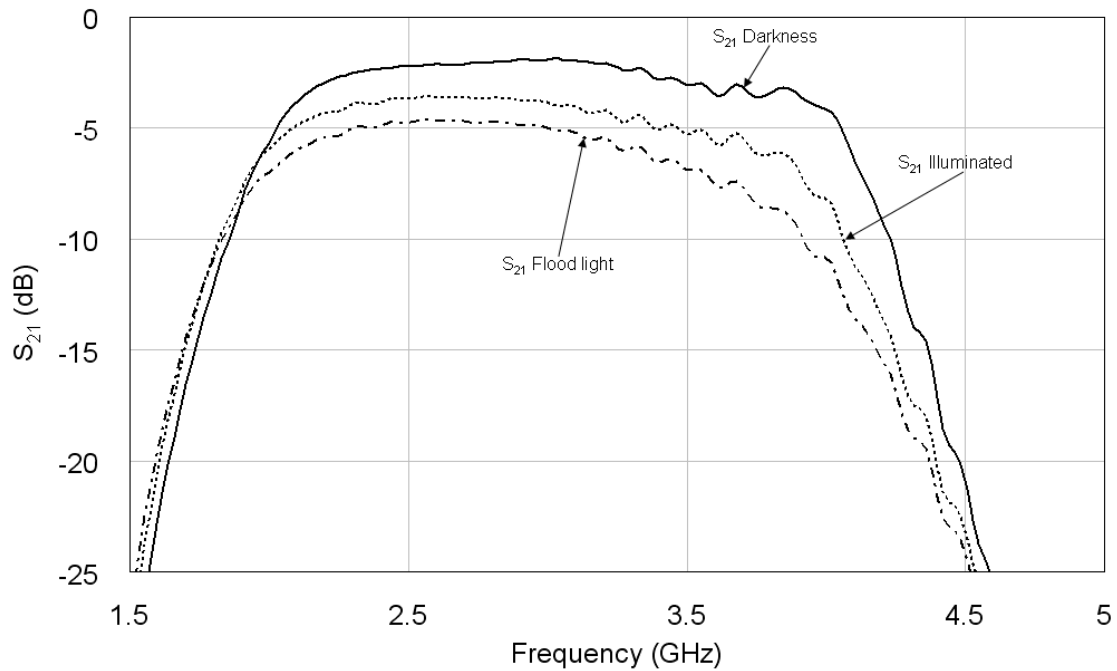
Figure 6.3 Measurement results for the optical tuneability experiment of a 4 x 1 EBG filter.

The effect can be explained by considering the illuminated area of the HRS to provide a lossy connection from the transmission line to ground, rather than adding capacitances. Several steps could be taken to improve this initial test, in order to achieve the desired results:

- A thinner HRS piece could be used in order to increase the capacitance.

- The HRS could be incorporated into the design to remove the influence of the air gap.

- A mask or a pattern on the HRS could be employed in order to control the location of the tuneable component and to remove unwanted connections to ground.

6.2 Tuneability With Micro Electromechanical Systems

For electrostatic actuation of MEMS switches, a displacement of 1 / 3 of the up-state distance causes snap down [58]. Therefore, the low frequency behaviour of the monolithic EBG structure is only continuously tuneable with MEMS capacitances in a narrow frequency range. If there is the need for binary switching, then comparing the up-state and the snap down case provides the largest frequency shift. Figure 5.4 shows the simulation results of the up-state of the 9 x 1 monolithic EBG structure and of the snap down case. The original gap width of 3 μm has been reduced to 100 nm for the snap down simulation. It can be seen that the low frequency peak and the rise of the passband has shifted towards lower frequencies with decreasing gap width.
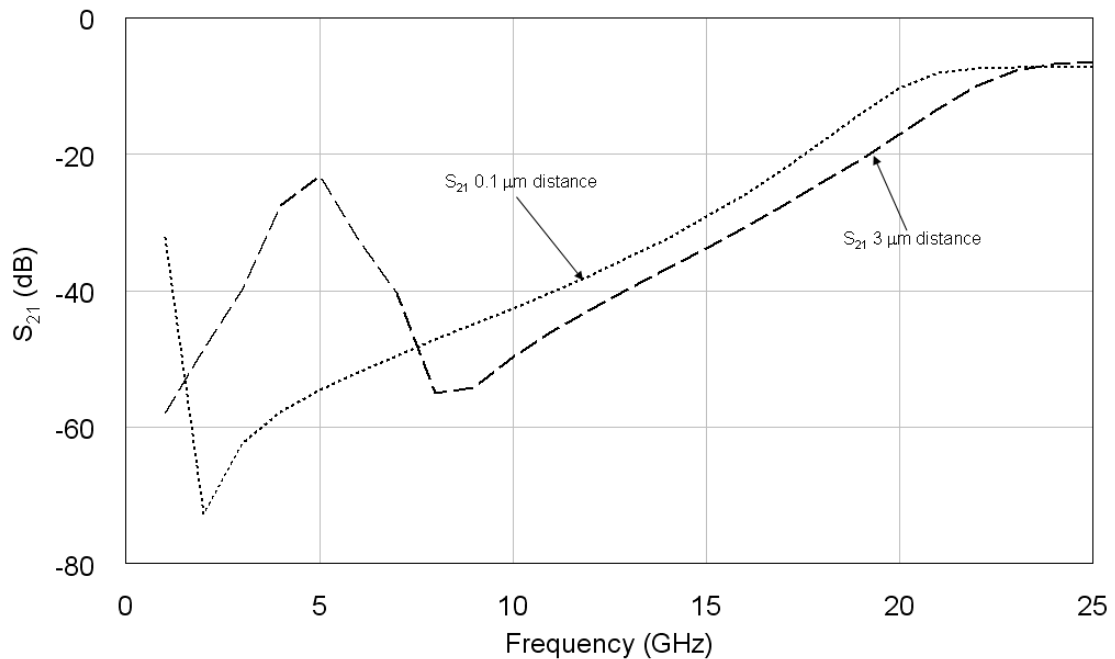
Figure 6.4 Comparison of insertion losses of the monolithic EBG structure for simulated up-state and snap down of MEMS tuneable capacitors.

79

6.3 Tuneability With Monolithic Microwave Integrated Circuits

In adaptive frequency division multiplexed systems, when channels either drop out or reduce their data rates, the remainder can be shuffled down to minimise spectral occupancy. As a result, the reduced transmission bandwidth will enable the power amplifier to be re-tuned for higher output power and/or greater efficiency. For example, the filter in a tuneable receiver filter (located after the low noise amplifier) that can significantly reduce its upper cut-off frequency will be able to minimise the input noise level into the rest of the receiver. The overall end-to-end carrier / noise ratio is thus significantly improved.

In recent years, efforts have been made to create standards for cognitive radio and dynamic spectrum access [59]. Economic models on the aspect of spectrum trading in cognitive radio networks have been investigated [60], which suggests that the importance of cognitive radio networks is going to increase. For applications that require dynamic spectrum access, filters with a tuneable bandwidth are needed. With conventional filter technologies, this can be achieved with the use of multiple tuning elements. However, this approach may not be simple in practice. An alternative approach is adopted here, using a planar EBG filter, with an integrated tuneable cell defect.

6.3.1 Monolithic Microwave Integrated Circuits

With the transmission through line, EBG arrays and ground bars electrically connected at direct current (DC), it is not easy to bias varactors directly, since additional DC blocking capacitors would be needed. Moreover, the sizes of the bias components may be comparable to the individual cells, which present a range of practical implementation

issues. Therefore, in order to avoid undue complexity, a unique solution had to be found. To this end, monolithic microwave integrated circuits (MMICs) were introduced; their be-spoke designs have integrated varactor diodes and associated bias circuitry. The design of the MMIC can be seen in Figure 6.5 (a), while the corresponding microphotograph of the chip can be seen in Figure 6.5 (b). The MMIC can be easily bonded directly onto a cell, using conductive epoxy glue, and then wire-bonded to the transmission line of the filter; thereby providing additional and tuneable series capacitance between the "defective" cell and the transmission line.
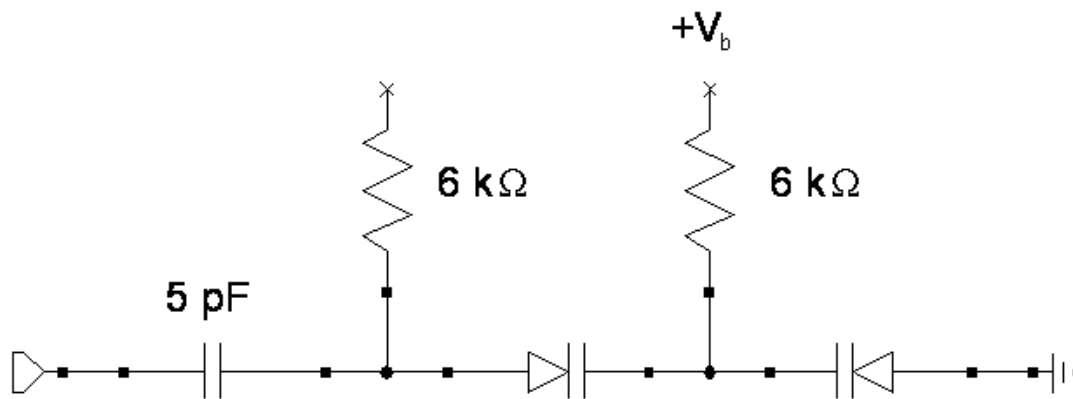
(a)
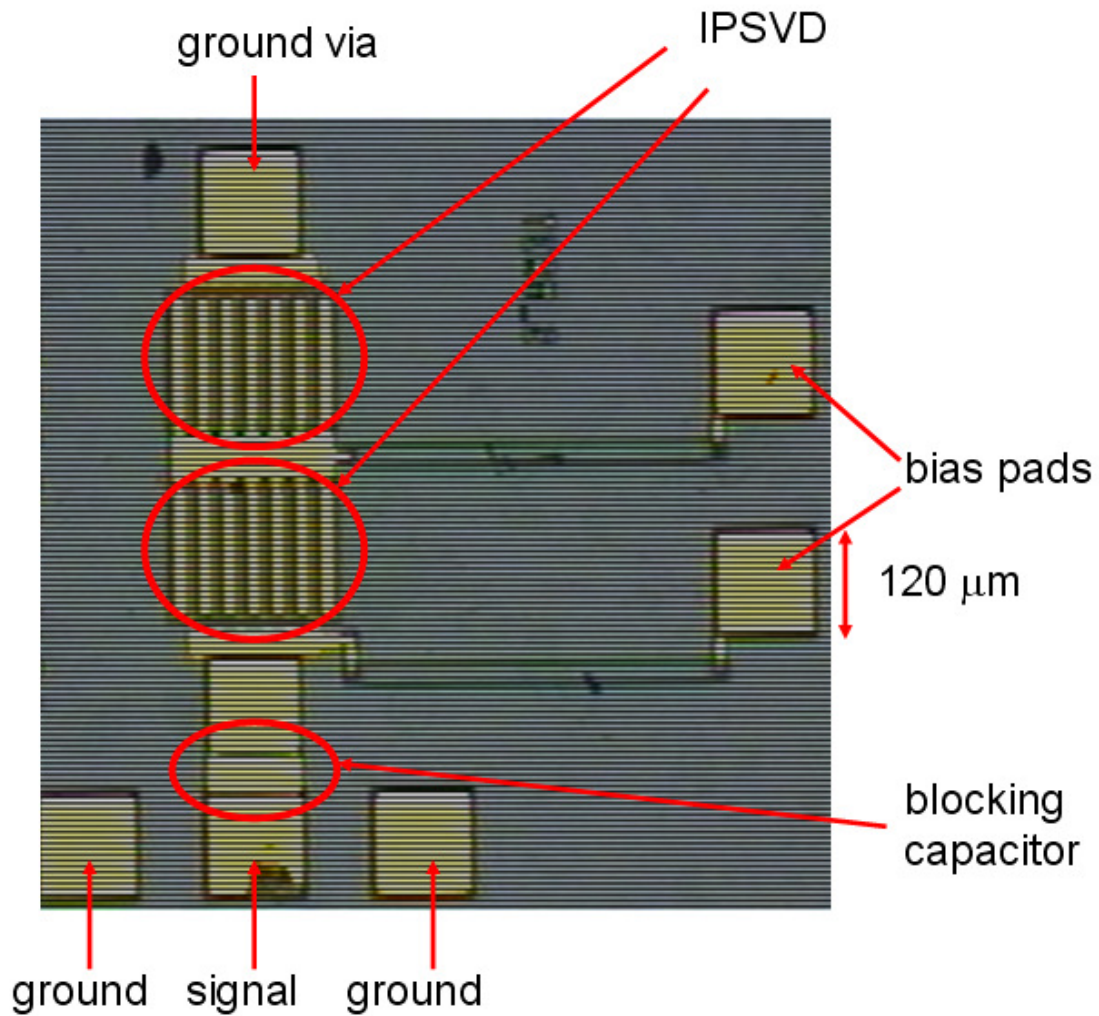
(b)

Figure 6.5 (a) MMIC design [61] and (b) Microphotograph of the realized MMIC [61].

A hybrid approach was adopted for the overall 2D equivalent circuit model of the filter, whereby the defective cell was represented by an equivalent circuit model of the MMIC in conjunction with a 3-port 3D electromagnetic model for a non-defective cell. In addition, a bond wire model (consisting of a series inductor and resistor, having frequency-dependant values) was also needed. Detailed equivalent circuit modelling of the MMIC had to be undertaken using information previously published [61]-[65]. The GaAs MMICs include two interdigitated planar Schottky varactor diodes (IPSVDs),

each having a gate periphery of 6 x 120 μm [61], with the basic model being previously

published [62],[63]. The element values were then scaled according to empirical results

[63]. Figure 6.6 (a) gives the equivalent circuit model for the complete MMIC, with that

for the individual IPSVD shown in Figure 6.6 (b).

(a)

(b)
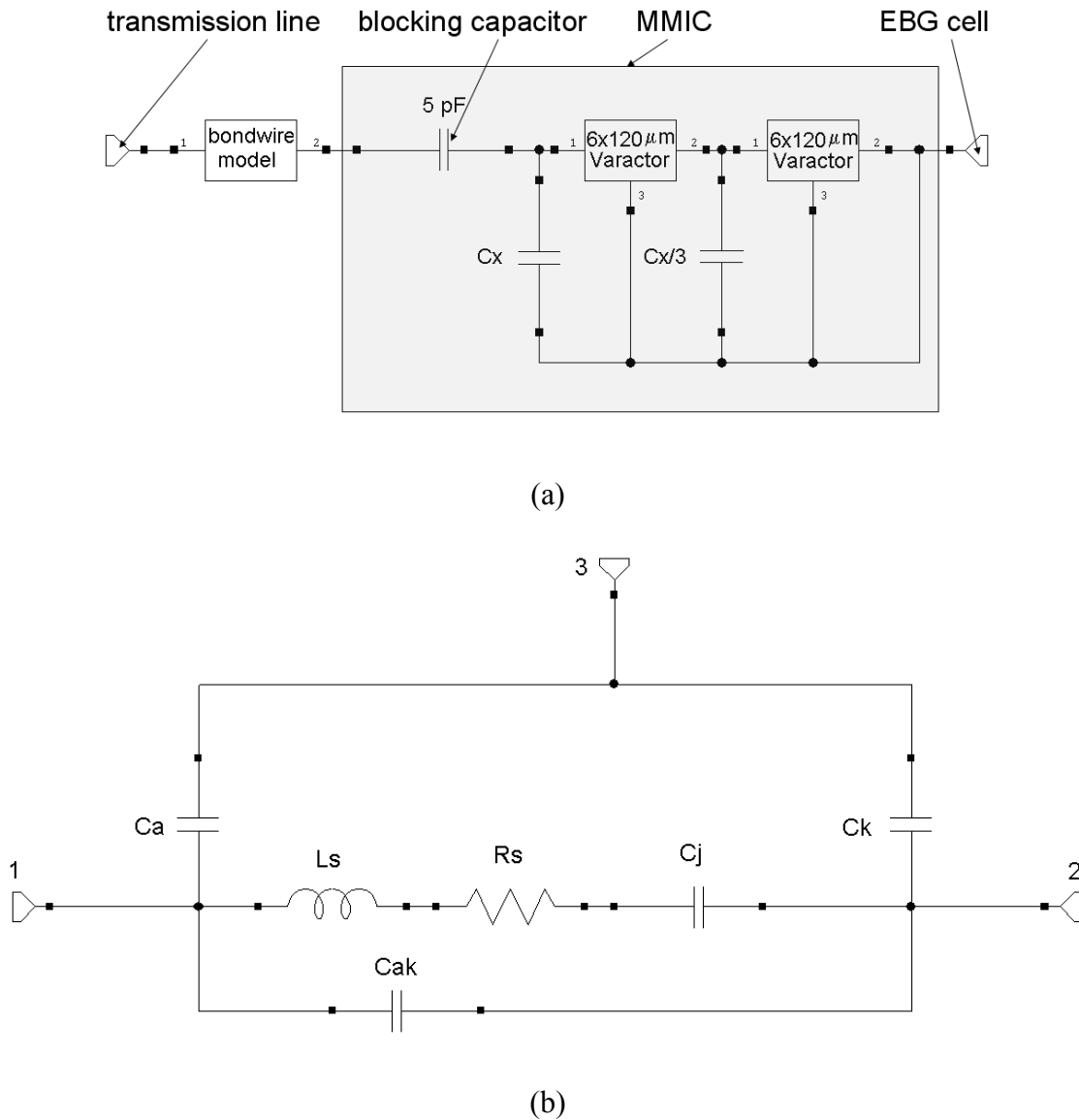
Figure 6.6 (a) equivalent circuit model for the complete MMIC [62],[63] and (b)

equivalent circuit model for the varactor [62],[63].

The ground plane of the MMIC can act as its own port terminal. As such, this 1-

port MMIC can be treated as a 2-port component. Here, the 1-port measurement (i.e.

s1p) files of the MMIC were converted into 2-port (i.e. s2p) files, by mapping the

83

ground of the 1-port file to a signal port in Agilent's Advanced Design System (ADS) software. The MMIC's equivalent circuit model results are in good agreement with those of the 2-port 'measurements'. Having said this, two of the scaled element values were tweaked to provide a better fit. Both the scaled values and the adjusted values are given in Table 6.1. The discrepancies between the scaled element values and those fitted to the measurements can be explained by the fact that the scaling laws only represent an approximation.

Table 6.1 MMIC Equivalent Circuit Element Values [63]

Component	Scaled Value	Adjusted Value
Cx	0.02 pF	-
Ca	0.0008 pF	-
Cak	0.024 pF	-
Cj	0.924 pF	1.25 pF
Ck	0.008 pF	-
Ls	0.02 nH	0.2 nH
Rs	3 Ω	-

6.3.2 Tuneable Cell Defect Filter

With the initial 2D equivalent circuit modelling approach, ideal tuneable capacitors were introduced, instead of the complete MMIC model, at different locations. The best results were obtained when the two variable capacitors were introduced between the transmission line and a connecting cell. Since the existing coupling capacitors between cells have a capacitance of ~ 2 fF, this series capacitive coupling between cells is negligible. As a result, the model can be further simplified to that depicted in Figure 6.7.
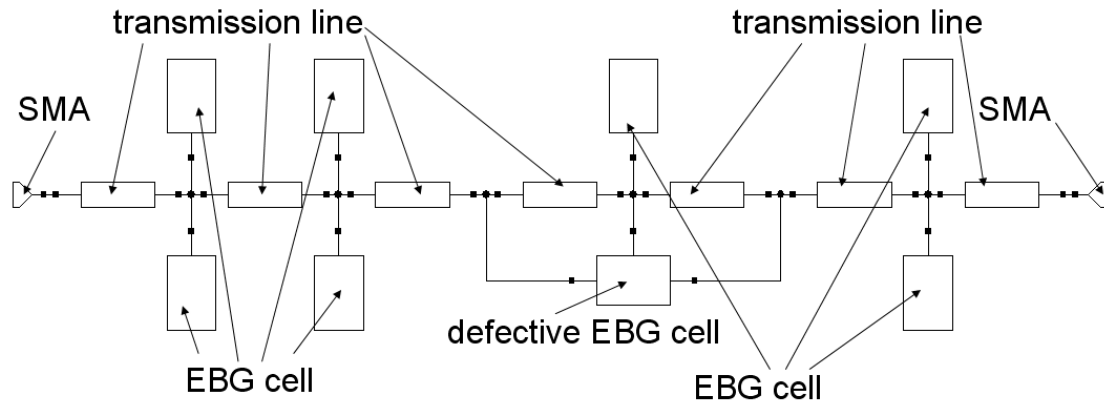
Figure 6.7 Simplified hybrid 2D Equivalent Circuit Model for the PCB version of the modified UC-EBG 4 x 1 cell array filter.

The PCB has an effective (fitted) dielectric loss tangent $tan\delta = 0.04$. The transmission line segments each have a width of 550 µm.

The EBG cells consist of a capacitance to ground of 5.6 pF and the four meandered inductors, three of which are grounded and one connects the cell to the transmission line. The meanders were modelled by transmission lines of 200 µm width and effective (fitted) length of 15.77 mm.

In order to implement a tuneable band-pass filter, two MMICs were placed in parallel with the series coupling capacitances between the transmission line and one adjacent cell. The MMICs were attached onto this cell using EPO-TEK$^{®}$ H20E-175 conductive epoxy glue. Bond wires also connect the MMIC to the transmission line. Figure 6.8 shows a 4 x 4 cell array version of the modified UC-EBG filter under test. For this prototype design, dc probe needles were attached to the MMICs in order to provide the bias voltage for the varactors.
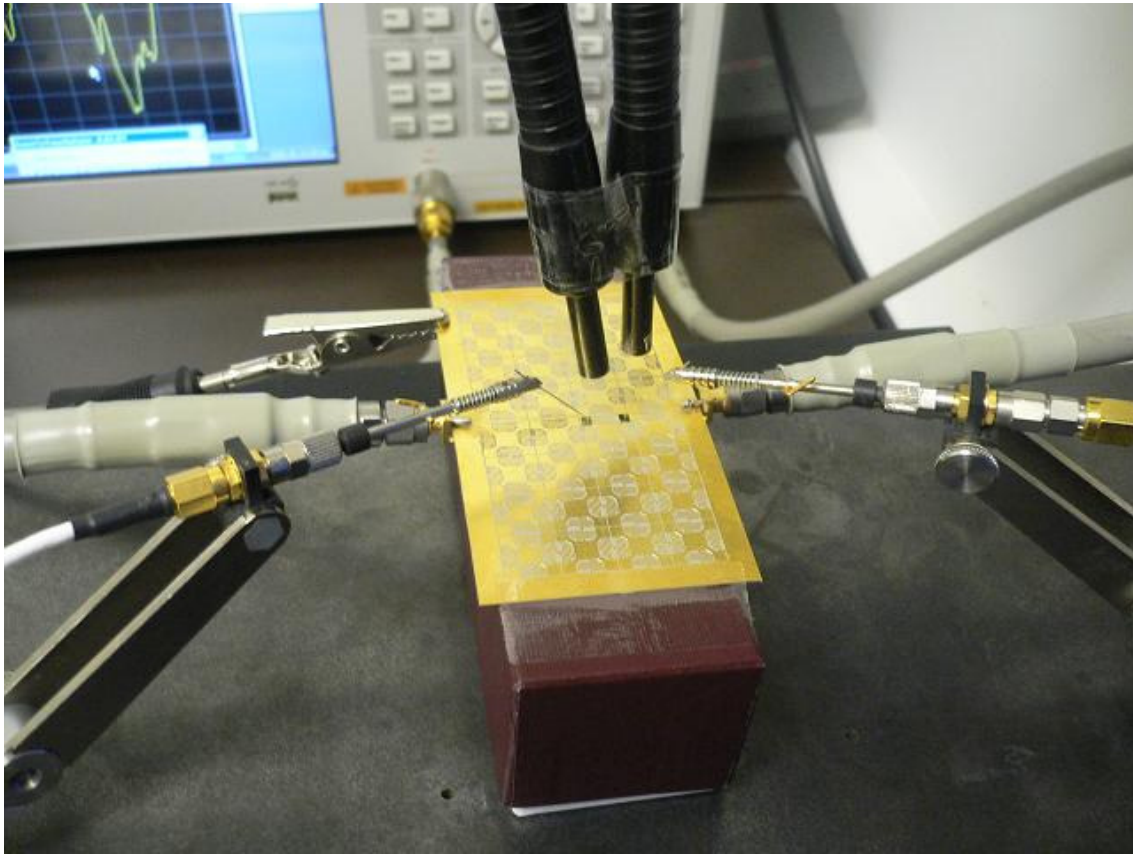
Figure 6.8 A 4 x 4 cell array version of the modified UC-EBG filter under test.

Since the varactors within the MMIC have a much larger capacitance (~ 1 pF) than the previously omitted series coupling capacitances (~ 2 fF), the influence of this path can no longer be overlooked. Figure 6.7 includes the two additional paths for the modified UC-EBG cell. Although the hybrid modelling approach can be further improved, an excellent match between measurement and simulations was achieved when the complete filter is modelled using only equivalent circuit modelling techniques. Figure 6.9 - Figure 6.13 show the measurements and the corresponding simulation results for the different varactor bias voltages.
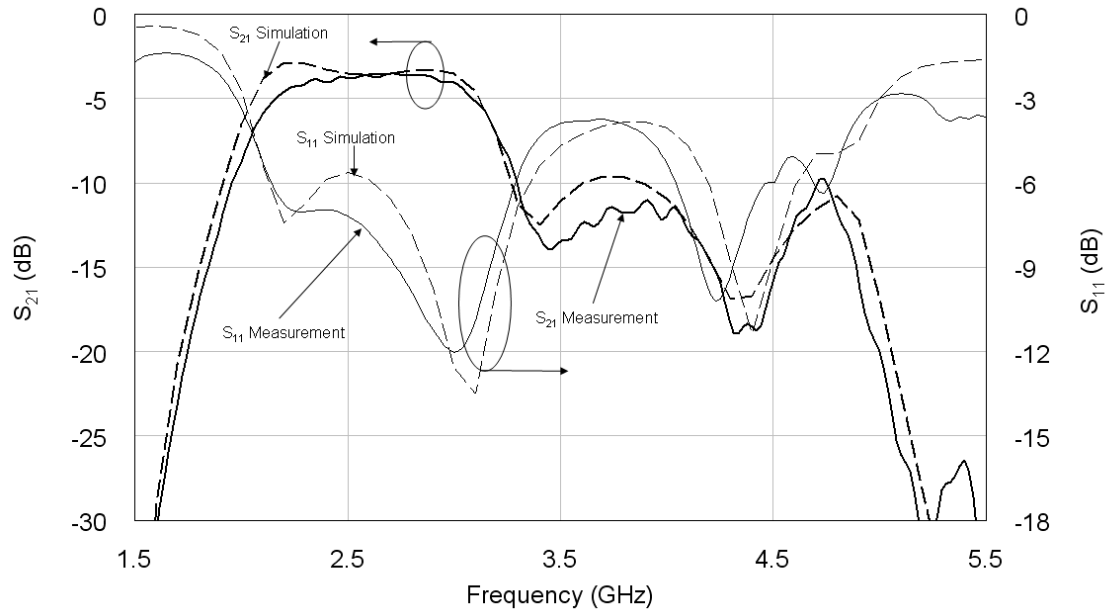
Figure 6.9 Measured filter behaviour at 0 V varactor bias voltages and simulated filter behaviour (C_j = 1.25 pF).
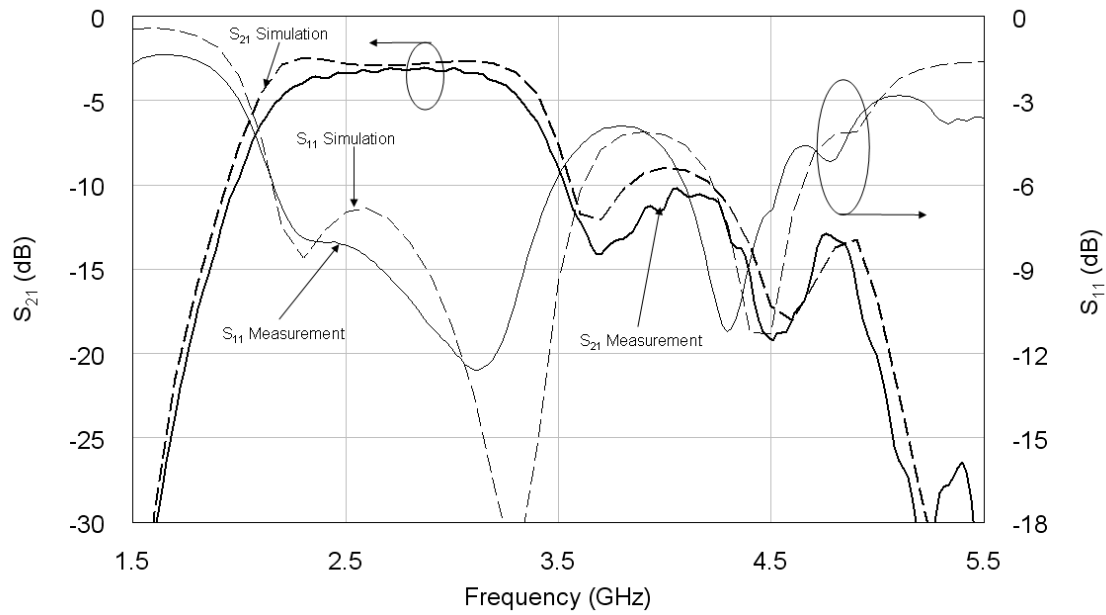
Figure 6.10 Measured filter behaviour at 0.5 V varactor bias voltages and simulated filter behaviour (C_j = 0.79 pF).
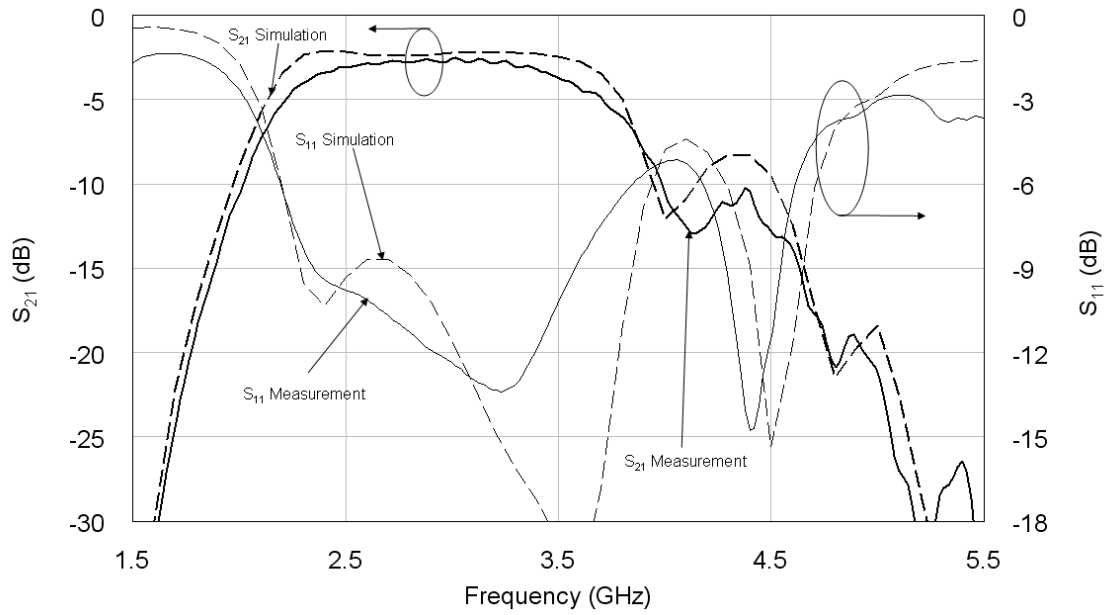
Figure 6.11 Measured filter behaviour at 1.5 V varactor bias voltages and simulated filter behaviour ($C_j = 0.47$ pF).
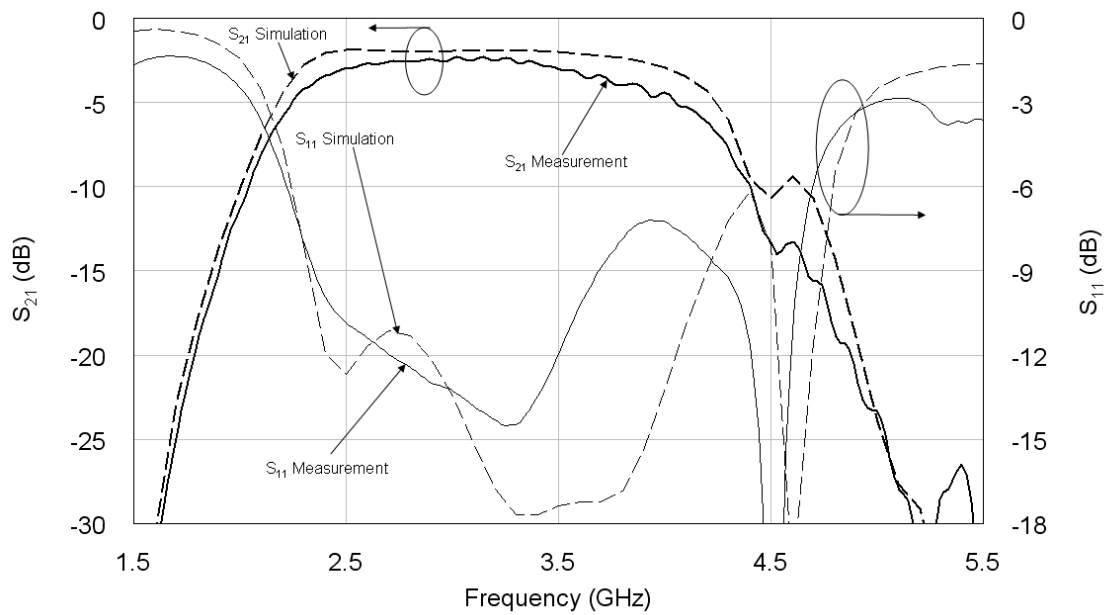
Figure 6.12 Measured filter behaviour at 3 V varactor bias voltages and simulated filter behaviour ($C_j = 0.26$ pF).
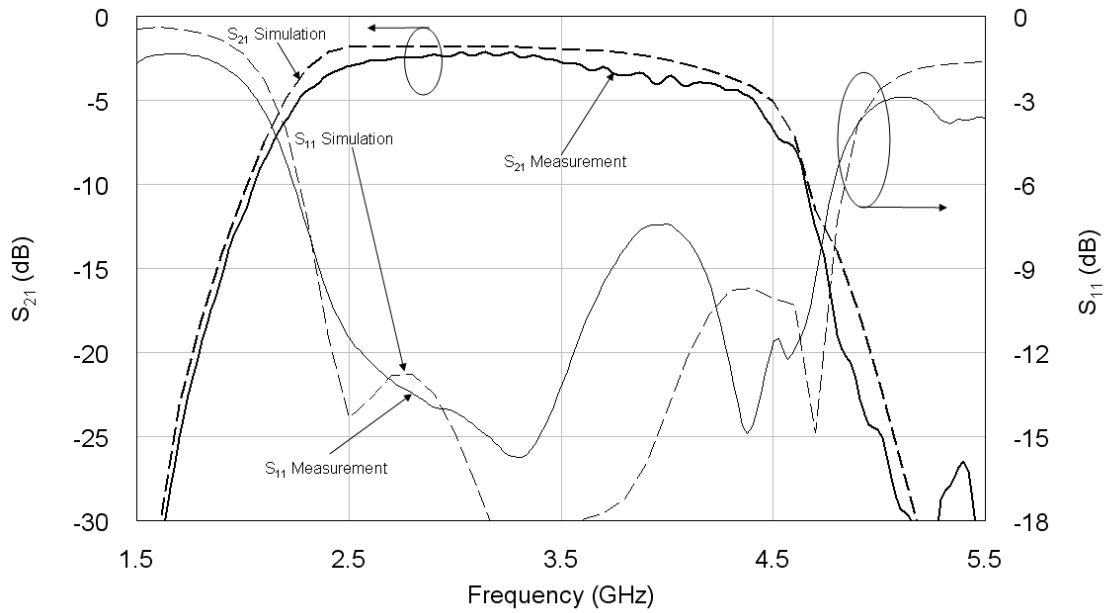
Figure 6.13 Measured filter behaviour at 8 V varactor bias voltages and simulated filter behaviour ($C_j = 0.18$ pF).

Here, the results for five different varactor bias voltages (from 0 to 8 V) are presented, to demonstrate the 2:1 3dB bandwidth tuneability of this filter. With increasing bias voltage, the junction capacitances of the IPSVDs decrease. Towards higher voltages, the depletion region reaches saturation. At that stage, the varactors have reached their lowest capacitance value.

Figure 6.14 shows the measured tuning behaviour for the centre frequency, bandwidth and fractional bandwidth of the passband. As expected, the centre frequency, fractional bandwidth and bandwidth increase with increasing IPSVD bias voltage, up to the saturation, which is reached at a voltage of roughly > 5V.
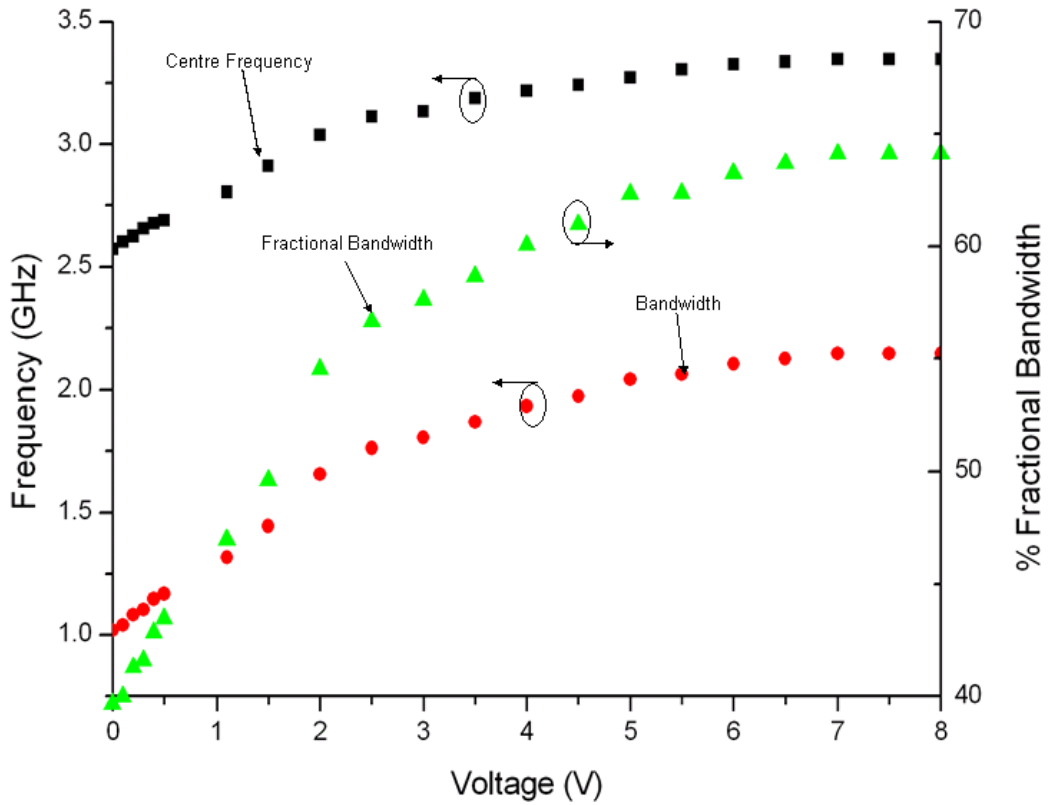
Figure 6.14 Measured tuning behaviour for the centre frequency, 3dB bandwidth and fractional bandwidth of the passband.

6.4 Summary

Different experiments were conducted to create tuneable EBG filters. A bandwidth tuneability of 2:1 has been achieved with the PCB filter, by introducing a single-cell defect employing two MMICs. Simulations have confirmed that the extent of the tuneability is not due to an increased coupling capacitance between the transmission line and the EBG cell, but due to the creation of additional signal paths and the distributed transmission line behaviour of the cell.

Following the initial work of the prototype monolithic filter, the next step is to introduce some form of tuneability. This could combine both single-cell defects and RF MEMS tuneable shunt capacitance in each cell. Tuning the latter would mainly

influence the low frequency behaviour of the passband, due to its effect on the second transmission zero. With the additional tuning of the high frequency behaviour of the passband, provided by the single cell defect, the complete passband could be made tuneable.

7 Summary and Outlook

The thesis investigated EBG structures and their application as high frequency band-pass filters. The following sections summarize the specific aspects that were analyzed, the results of the experiments and the conclusions that were reached. The end of this chapter maps out directions for future research on this topic.

7.1 The Modified Uniplanar Compact Electromagnetic Bandgap Cell

In the introduction, an overview of the different types of EBGs was given. For microwave applications, the planar EBGs are of particular importance. Among them, the mushroom EBG and the UC-EBG are the most important types.

The thesis takes a closer look at the UC-EBG and investigates a modified version with increased inductive coupling between the cells. The increase stems from an exchange of the straight connection between cells with meandered lines.

The eigenmode solver of HFSS™ helped to determine the dispersion diagram of the modified UC-EBG. The dispersion diagram confirmed that the TM bandgap appeared between 1.5 GHz and 5.5 GHz.

With the results of the characterisation of the modified UC-EBG, the implementation of a filter consisting of the modified UC-EBG could be investigated.

7.2 Printed Circuit Board Electromagnetic Bandgap Filter Implementation

EBG filter applications on PCB typically consisted of a microstrip transmission line with the EBG pattern underneath it on the ground plane. The filter implementation presented in this thesis follows a different approach: The microstrip transmission line is connected to EBG arrays on both sides. The ground plane remains unchanged, a uniform metal surface. The edges of the EBG array are connected to the ground plane by vias. EM waves with frequencies inside of the forbidden band of the EBG cannot propagate through the EBG and therefore propagate along the transmission line. At other frequencies the EBG array provides a signal path to ground, thus attenuating signal propagation along the line.

A 2D equivalent circuit model of the structure was created, which fits the measured filter response. Other filter implementations with additional EBG cells could be accurately described with this 2D model as well.

This filter concept uses the previously characterised modified UC-EBG cell. A 3D electromagnetic model of the structure was created in HFSS™. The simulation predicts the filter behaviour, which is in good agreement with the measurements of the manufactured PCB prototype.

7.3 Monolithic Electromagnetic Bandgap Structure

With the concept of the filter successfully proven, scaling of the design is the next logical step. By scaling down the size of the EBG cells, the passband of the filter can be shifted towards higher frequencies. Due to the limited resolution of PCB etching, different technologies had to be used for the scaling process. The device was micromachined on a wafer, allowing for significantly reduced feature sizes. The

production of the monolithic EBG structure was part of two different multi project wafer runs, which posed the additional challenge of designing a device to someone else's parameters.

The monolithic approach to build the structure is of particular interest due to its compatibility with commercial fabrication processes.

The structure was designed with the possibility of MEMS tuneability in mind, something that was further investigated with simulations as detailed in the previous chapter.

7.4 Tuneable Electromagnetic Bandgap Filters

After the characterisation of the EBG cell and the implementation of the EBG filter, the possibility of adding tuneable components to the filters was investigated. An experiment that revolved around optical excitation of carriers in HRS did not yield the desired results. Nevertheless, the experiment was still important, as it highlighted the challenges associated with this method. Several improvements to overcome the encountered difficulties were formulated.

Simulations were carried out to predict the influence of MEMS tuneable shunt capacitances for the monolithic EBG structure. These simulations confirm that the location and incline of the rise of the passband can be controlled by varying the shunt capacitance.

Finally, the effect of single defects on the filter response was investigated. MMICs were added to one cell of the PCB EBG and connected to the transmission line with bond wires. By varying the bias voltage of varactors within the MMICs, the bandwidth of the filter could be tuned.

94

7.5 Future Work

The results from this thesis provide the stepping stones for several areas of investigation regarding planar EBGs and their applications. The following three sections list a few ideas in order to outline possible general directions of future research in this field.

7.5.1 Fundamentals

The series capacitance between cells could be increased, so that its influence is no longer negligible. To this end, the use of fractal capacitors could be investigated.

Changing the meander geometry is going to change the inductance. However, a change of the meander geometry is also going to alter the available space for the main part of the cell and thus affect the size of the shunt capacitance. This relation could be investigated with the aim of finding an optimized meander / main part of the cell ratio for a specific band gap.

7.5.2 Tuneability

Further experiments to implement optical tuneability of the PCB EBG filter need to be carried out, to verify the suggestions for improvement of the method.

The different tuneability methods could be optimized not only for performance and real estate usage, but also regarding their associated production cost.

By combining the two tuning approaches of introducing defects into the cells as well as including MEMS tuneable shunt capacitances, an EBG filter can be designed with a tuneable passband that can shift bandwidth and centre frequency independently from each other.

7.5.3 Applications

The simulation results on MEMS tuneable shunt capacitance for the monolithic EBG structure would also be of use for designing reflect array applications with the EBG cells.

Another different application of the EBG cells would be to investigate their suitability as FSS.

Papers From This Research

1. K. Herbertz and S. Lucyszyn, "Two-Dimensional Metamaterials for Dual-Band Filter Applications," *38th European Microwave Conference*, pp. 1366 – 1369, Oct. 2008

2. K. Herbertz and S. Lucyszyn, "EBG Filter with Single-Cell MMIC-Tuneable Defect," *IET Microwaves, Antennas and Propagation,* vol. 4, no. 8, pp. 1123 - 1131, Aug. 2010

Bibliography

[1]   N. Engheta, R. W. Ziolkowski, *Metamaterials Physics and Engineering Explorations*, 1st ed., John Wiley & Sons, Inc., 2006

[2]   V. G. Veselago, "The electrodynamics of substances with simultaneously negative value of ε and μ," *Soviet Phys Uspekhi*, vol. 10, no. 4, pp. 509-514, Jan-Feb. 1968

[3]   J.B. Pendry, A.J. Holden, D.J. Robbins, and W.J. Stewart, "Magnetism from conductors and enhanced nonlinear phenomena," *IEEE Transactions on Microwave Theory and Techniques*, vol. 47, no. 11, pp. 2075 - 2084, 1999

[4]   C. Caloz and T. Itoh, *Electromagnetic Metamaterials Transmission Line Theory and Microwave Applications*, 1st ed., John Wiley & Sons, Inc., 2006

[5]   E. Yablonovitch, "Photonic Band-Gap Structures," *Journal Optical Society of America*, vol. 10, no. 2, pp. 283 – 295, Feb. 1993

[6]   E. Yablonovitch, "Inhibited Spontaneous Emission in Solid-State Physics and Electronics," *Physical Review Letters*, vol. 58, no. 20, pp. 2059 – 2062, May 1987

[7]   D. F. Sievenpiper, M.E. Sickmiller, and E. Yablonovitch, "3-D metallic photonic bandgap structures," *Conference on Lasers and Electro-Optics*, 1996

[8]   Y. Fei-Ran, M. Kuang-Ping, Q. Yongxi, and T. Itoh, "A uniplanar compact photonic-bandgap (UC-PBG) structure and its applications for microwave circuit," *Microwave Theory and Techniques, IEEE Transactions*, vol. 47, no. 8, pp. 1509 – 1514, Aug. 1999

[9]   D. Sievenpiper, L. Zhang, R.F.J. Broas, N.G. Alexopolus, and E. Yablonovitch, "High-impedance Electromagnetic Surfaces with a Forbidden Frequency Band," *IEEE Trans. Microwave Theory Tech.*, vol. 47, no. 11, pp. 2059 – 2074, Nov. 1999

[10] R. Coccioli, F.R. Yang, K.P. Ma, and T. Itoh, "Aperture-Coupled Patch Antenna on UCPBG substrate," *IEEE Transactions on Microwave Theory and Techniques*, vol. 47, no. 11, pp. 2123 – 2130, Nov. 1999

[11] S.K. Sharma and L. Shafai, "Enhanced Performance of an Aperturecoupled Rectangular Microstrip Antenna on a Simplified Unipolar Compact Photonic Bandgap (UC-PBG) Structure," *IEEE Antennas and Propagation Society International Symposium*, vol. 2, pp. 498 – 501, 2001

[12] Y. Li, F. Zhenghe, C. Fanglu, and F. Mingyan, "A novel compact electromagnetic band-gap (EBG) structure and its application in microstrip antenna arrays," *Microwave Symposium Digest, IEEE MTT-S International*, vol. 3, pp. 1635 – 1638, Jun. 2004

[13] C. Jinwoo, V. Govind, and M. Swaminathan, "A novel electromagnetic bandgap (EBG) structure for mixed-signal system applications," *IEEE Radio and Wireless Conference*, pp. 243 – 246, 2004

[14] Y. Li, F. Mingyan, and F. Zhenghe, "A spiral electromagnetic bandgap (EBG) structure and its application in microstrip antenna arrays," *Microwave Conference Proceedings, Asia-Pacific Conference Proceedings*, vol. 3, Dec. 2005

[15] B. Lin, Q. Zheng, and N. Yuan, "A novel planar PBG structure for size reduction," *IEEE Microwave and Wireless Components Letters*, vol. 16, no. 5, pp. 269 – 271, 2006

[16] K. Herbertz and S. Lucyszyn, "Two-Dimensional Metamaterials for Dual-Band Filter Applications," *38th European Microwave Conference*, pp. 1366 – 1369, Oct. 2008

[17] E.R. Brown, C.D. Parker, and E. Yablonovitch, "Radiation Properties of a planar antenna on a photonic-crystal substrate," *Journal Optical Society of America*, vol. 10, no. 2, pp. 404 – 407, Feb. 1993

[18] L. Zhan and Y. Rahmat-Samii, "PBG, PMC and PEC ground planes: a case study of dipole antennas," *Antennas and Propagation Society International Symposium, IEEE*, vol. 2, pp. 674 – 677, Jul. 2000

[19] R.S. Jong, T. Heung-Sik, L. Jae-Gon, and L. Jeong-Hae, "Comparative analysis of four types of high-impedance surfaces for low profile antenna applications," *Antennas and Propagation Society International Symposium*, vol. 1A, pp. 758 – 761, Jul. 2005

[20] Y. Fei-Ran, M. Kuang-Ping, Q. Yongxi, and T. Itoh, "A novel TEM waveguide using uniplanar compact photonic-bandgap (UC-PBG) structure," *Microwave Theory and Techniques, IEEE Transactions*, vol. 47, no. 11, pp. 2092 – 2098, Nov. 1999

[21] M. Belaid and W. Ke, "Spatial power amplifier using a passive and active TEM waveguide concept," *Microwave Theory and Techniques, IEEE Transactions*, vol. 51, no. 3, pp. 684 – 689, Mar. 2003

[22] V. Radisic, Y. Qian, R. Coccioli, and T. Itoh, "Novel 2-D photonic bandgap structure for microstrip lines," *IEEE Microwave and Guided Wave Letters*, vol. 8, no. 2, pp. 69 - 71, 1998

[23] I. Rumsey, M. Piket-May, and P.K. Kelly, "Photonic bandgap structures used as filters in microstrip circuits," *IEEE Microwave and Guided Wave Letters*, vol. 8, no. 10, pp. 336 - 338, 1998

[24] S. Y. Huang and Y.H. Lee, "A novel dual-plane compact electromagnetic band-gap (DPC-EBG) filter design," *IEEE Proceedings 4th International Conference on Microwave and Millimeter Wave Technology, ICMMT*, pp. 468 - 471, 2004

[25] Wei Wang, Xiang-yu Cao, Wan-yin Zhou, and Tao Liu, "A novel low-pass filter using uniplanar compact electromagnetic-bandgap (UC-EBG) structure," *IEEE Proceedings 4th International Conference on Microwave and Millimeter Wave Technology, ICMMT*, pp. 476 - 479, 2004

[26] Y. Fei-Ran, Q. Yongxi, and T. Itoh, "A novel uniplanar compact PBG structure for filter and mixer applications," *IEEE MTT-S International Microwave Symposium Digest*, vol. 3, pp. 919 - 922, 1999

[27] G. Chu, C. Zhi Ning, W. Yun Yi, Y. Ning, and Q. Xian Ming, "Study and suppression of ripples in passbands of series/parallel loaded EBG filters," *IEEE Transactions on Microwave Theory and Techniques*, vol. 54, no. 4, pp. 1519 - 1526, 2006

[28] C. Kittel, *Introduction to solid state physics,* 8th ed., Wiley, 2005

[29] Joannopoulos, J. D., Meade, R. D., and Winn, J. N., *Photonic crystals : molding the flow of light***,** Princeton, N.J. : Princeton University Press, 1995

[30] http://www.applet-magic.com/brillouin.htm (Accessed March 2010)

[31] R. C. Rumpf, *Design and optimization of nano-optical elements by coupling fabrication to optical behavior*, Ph.D. thesis, 2006

[32] F. Yang and Y. Rahmat-Samii, *Electromagnetic Band Gap Structures in Antenna Engineering*, Cambridge University Press, 2009

[33] Y. Yao, X. Wang, and Z. Feng, "A Novel dual-band Compact Electromagnetic Bandgap (EBG) Structure and its Application in multi-antennas," *IEEE Antennas and Propagation Society International Symposium*, pp. 1943-1946, 2006

[34] A. Aminian, F. Yang, and Y. Rahmat-Samii, "In-phase reflection and EM wave suppression characteristics of electromagnetic band gap ground planes," *IEEE Antennas and Propagation Society International Symposium*, vol. 4, pp. 430 - 433, 2003

[35] Y. Wang, J. Huang, and Z. Feng, "A Novel Fractal Multi-Band EBG Structure and Its Application in Multi-Antennas," *IEEE Antennas and Propagation Society International Symposium*, pp. 5447 - 5450, 2007

[36] L. Brillouin, *Wave Propagation in Periodic Structures: Electric Filters and Crystal Lattices*, New York: McGraw-Hill, 1946

[37] L. Zhang, N.G. Alexopoulos, D. Sievenpiper, E. Yablonovitch, "An Efficient Finite-Element Method for the Analysis of Photonic Band-Gap Materials," *Microwave Symposium Digest, IEEE MTT-S International*, vol. 4, pp. 1703 − 1706, Jun. 1999

[38] Y. Zhou and S. Lucyszyn, "HFSS™ Modelling Anomalies with THz Metal-Pipe Rectangular Waveguide Structures at Room Temperature," *PIERS Online*, vol. 5, no. 3, pp. 201-211, 2009

[39] J. D. Rhodes, *Theory of Electrical Filters*, John Wiley & Sons Ltd., 1976, reprinted 2002

[40] W. J. Karl, *Piezomagnetic Thin-Films and Devices*, Ph.D. thesis, 2005

[41] F. W. Grover, *Inductance Calculations*, Van Nostrand, 1946, reprinted by Dover Publications, ISBN 0486495779, 2004

[42] H. M. Greenhouse, "Design of Planar Rectangular Microelectronic Inductors," *IEEE T. Parts Hyb. Pac.* 10 (2), 1974

[43] K. Herbertz and S. Lucyszyn, "EBG Filter with Single-Cell MMIC-Tuneable Defect," *IET Microwaves, Antennas and Propagation,* vol. 4, no. 8, pp. 1123 - 1131, Aug. 2010

[44] http://www.trackwise.co.uk/ (Accessed March 2010)

[45] Personal communication with Conrad Bailey, Nov. - Dec. 2007

[46] G.M. Rebeiz, *RF MEMS - Theory, Design, and Technology*, John Wiley & Sons, Inc., p. 29, 2003

[47] E. Ozbay, K. Aydin, S. Butun, K. Kolodziejak, and D. Pawlak, "Ferroelectric Based Tuneable SRR Based Metamaterial for Microwave Applications," *37th European Microwave Conference*, pp. 497 – 499, Oct. 2007

[48] A. Velez, J. Bonache, and F. Martin, "Varactor-Loaded Complementary Split Ring Resonators (VLCSRR) and Their Application to Tunable Metamaterial Transmission Lines," *IEEE Microwave and Wireless Components Letters*, vol. 18, no. 1, pp. 28 – 30, Jan. 2008

[49] D. Kuylenstierna, E. Ash, A. Vorobiev, T. Itoh, and S. Gevorgian, "X-band Left Handed Phase Shifter using Thin Film $Ba_{0.25}SR_{0.75}TiO_3$ Ferroelectric Varactors," *36th European Microwave Conference*, pp. 847 – 850, Sep. 2006

[50] M.A.Y. Abdalla, K. Phang, and G.V. Eleftheriades, "Printed and Integrated CMOS Positive/Negative Refractive-Index Phase Shifters Using Tunable Active Inductors," *IEEE Transactions on Microwave Theory and Techniques*, vol. 55, no. 8, pp. 1611 – 1623, Aug. 2007

[51] C.L. Holloway, E.F. Kuester, J. Baker-Jarvis, P. Kabos, and M. Mohamed, "Double negative (DNG) index composite structure from non-conducting materials with an application to controllable surfaces," *Conference on Electrical*

Insulation and Dielectric Phenomena, CEIDP '04, 2004 Annual Report pp. 143 – 144, Oct. 2004

[52] T. Hand and S. Cummer, "Characterization of Tunable Metamaterial Elements Using MEMS Switches," *IEEE Antennas and Wireless Propagation Letters*, vol. 6, pp. 401-404, 2007

[53] A. Degiron, J.J. Mock, and D.R. Smith, "Optical Control of Metamaterial Unit Cells at Microwave Frequencies," *International Symposium on Signals, Systems and Electronics, ISSSE '07*, pp. 209 – 212, Jul. 2007

[54] L. Mercier, E. Rodes, J. Drouet, L. Leger, E. Arnaud, M. Thevenot, T. Monediere, and B. Jecko, "Steerable and tunable "EBG resonator antennas" using smart metamaterials," *IEEE Antennas and Propagation Society International Symposium*, pp. 406 – 409, Jul. 2006

[55] J.A. Bossard, Xiaotao Liang, Ling Li, Seokho Yun, D.H. Werner, B. Weiner, T.S. Mayer, P.F. Cristman, A. Diaz, and I.C. Khoo, "Tunable Frequency Selective Surfaces and Negative-Zero-Positive Index Metamaterials Based on Liquid Crystals," *IEEE Transactions on Antennas and Propagation*, vol. 56, no. 5, pp. 1308 - 1320, May 2008

[56] D. Draskovic and D. Budimir, "Optically reconfigurable matching networks," *International Topics Meeting on Microwave Photonics, 2008. Jointly held with the 2008 Asia-Pacific Microwave Photonics Conference. MWP/APMP 2008*, pp. 135 – 137, 2008

[57] J.C. Vardaxoglou, A. Chauraya, and P. de Maagt, "Reconfigurable electromagnetic band gap based structures with defects for mm wave and antenna applications," *Twelfth International Conference on Antennas and Propagation*, vol. 2, pp. 763 - 766, 2003

[58] O. Degani, E. Socher, A. Lipson, T. Lejtner, D.J. Setter, S. Kaldor, and Y. Nemirovsky, "Pull-in study of an electrostatic torsion microactuator," *Journal of Microelectromechanical Systems*, vol. 7, no. 4, pp. 373 - 379, 1998

[59] M. Sherman, A.N. Mody, R. Martinez, C. Rodriguez, and R. Reddy, "IEEE Standards Supporting Cognitive Radio and Networks, Dynamic Spectrum Access, and Coexistence," *IEEE Communications Magazine*, vol. 46, no. 7, pp. 72 − 79, Jul. 2008

[60] D. Niyato and E. Hossain, "Spectrum trading in cognitive radio networks: A market-equilibrium-based approach," *IEEE Wireless Communications*, vol. 15, no. 6, pp. 71-80, Dec. 2008

[61] S. Lucyszyn and I. D. Robertson, "Decade bandwidth hybrid analogue phase shifter using MMIC reflection terminations," *IEE Electronics Letters.*, vol. 28, no. 11, pp. 1064-1065, May 1992

[62] S. Lucyszyn, G. Green, and I. D. Robertson, "Accurate millimeter-wave large signal modeling of planar Schottky varactor diodes," *IEEE MTT-S Symposium Digest*, Albuquerque, USA, pp. 259-262, Jun. 1992

[63] S. Lucyszyn, G. Green, and I. D. Robertson, "Interdigitated planar Schottky varactor diodes for tunable MMIC applications," *Proceedings of the ESA/IEEE European Gallium Arsenide Applications Symposium (GAAS'92)*, ESTEC, Noordwijk, The Netherlands, Session 1B, Apr. 1992

[64] S. Lucyszyn, J. Luck, G. Green, and I. D. Robertson, "Enhanced modelling of interdigitated planar Schottky varactor diodes," *IEEE Asia-Pacific Microwave Conference (APMC'92)*, Adelaide, Australia, pp. 273-278, Aug. 1992

[65] S. Lucyszyn and I. D. Robertson, "Optically-induced measurement anomalies with voltage-tunable analog control MMICs," *IEEE Transactions on Microwave Theory Tech.*, vol. 46, no. 8, pp. 1105-1114, Aug. 1998

Appendix

Matlab Code

```matlab
close all;
clear all;
p = 1;                                      %period of the EBG in cm
w = 0.02.*p;                      %trackwidth based on the period, in cm
t = 0.0018;                                 %conductor thickness in cm
le = [0.05.*p 0.22.*p 0.04.*p 0.44.*p 0.04.*p 0.44.*p 0.04.*p 0.39.*p
0.04.*p 0.3.*p 0.04.*p 0.13.*p 0.035.*p]; %length of segments for self
inductance
L= 2.*le.* (log(2.*le./(w+t)) +0.50049 + ((w+t)./(3.*le)));       %self
inductance
Lself=sum(L);                                   %total self inductance
Lstraight= 2.*(sum(le)).* (log(2.* (sum(le))./(w+t)) +0.50049 +
((w+t)./(3.* (sum(le))))); %self inductance if it were a straight line
instead of a meander

Mpos = [1E-20.*p 0.22.*p 0.22.*p 0.08.*p; 0.17.*p 0.175.*p 1E-20*p
0.16.*p; 0.05.*p 0.39.*p 1E-20.*p 0.08.*p; 0.22.*p 0.13.*p 0.09*p
0.16.*p; 0.05.*p 0.3.*p 0.09.*p 0.08.*p; 0.17.*p 0.13.*p 0.09*p
0.08.*p;];  %positive mutual inductance matrix, each row lists size p,
size m, size q and distance d. The columns are M2,6 M2,10 M4,8 M4,12
M6,10 and M8,12
Mpossize=size(Mpos);

for i=1:Mpossize(1)
GMD(i) = exp ( log (Mpos(i,4)) -((1./12).*(Mpos(i,4)./w).^-2) -
((1./60).*(Mpos(i,4)./w).^-4) -((1./168).*(Mpos(i,4)./w).^-6) -
((1./360).*(Mpos(i,4)./w).^-8) -((1./660).*(Mpos(i,4)./w).^-10) );
                                %geometric mean distance between tracks

Qa = log (
((Mpos(i,1)+Mpos(i,2))./GMD(i))+(1+(((Mpos(i,1)+Mpos(i,2)).^2)./
(GMD(i).^2))).^(0.5)) - (1+( (GMD(i)).^2./(
(Mpos(i,1)+Mpos(i,2)).^2))).^(0.5)+(GMD(i)./ (Mpos(i,1)+Mpos(i,2)));
Qb = log (
((Mpos(i,2)+Mpos(i,3))./GMD(i))+(1+(((Mpos(i,2)+Mpos(i,3)).^2)./
(GMD(i).^2))).^(0.5)) - (1+( (GMD(i)).^2./(
(Mpos(i,2)+Mpos(i,3)).^2))).^(0.5)+(GMD(i)./ (Mpos(i,2)+Mpos(i,3)));
Qc = log ( (Mpos(i,1)./GMD(i))+(1+(( Mpos(i,1).^2)./
(GMD(i).^2))).^(0.5)) - (1+( (GMD(i)).^2./(
Mpos(i,1).^2))).^(0.5)+(GMD(i)./ Mpos(i,1));
Qd = log ( (Mpos(i,3)./GMD(i))+(1+(( Mpos(i,3).^2)./
(GMD(i).^2))).^(0.5)) - (1+( (GMD(i)).^2./(
Mpos(i,3).^2))).^(0.5)+(GMD(i)./ Mpos(i,3));

Mp(i)= (Mpos(i,1)+Mpos(i,2)).*Qa + (Mpos(i,2)+Mpos(i,3)).* Qb -
Mpos(i,1).* Qc - Mpos(i,3).*Qd;

end
Mpostotal=2.*(sum(Mp));                 %total positive mutual inductance

Mneg = [1E-20.*p 0.22.*p 0.22.*p 0.04.*p; 1E-20.*p 0.22.*p 0.17.*p
0.12.*p; 1E-20.*p 0.13.*p 0.09.*p 0.20.*p; 1E-20.*p 0.44.*p 1E-20.*p
0.04.*p; 0.05.*p 0.30.*p 0.09.*p 0.12.*p; 1E-20.*p 0.39.*p 0.05.*p
0.04.*p; 0.22.*p 0.13.*p 0.09.*p 0.12.*p; 1E-20.*p 0.30.*p 0.09.*p
0.04.*p; 1E-20.*p 0.13.*p 0.17.*p 0.04.*p;];            %negative mutual
```

```matlab
inductance matrix, each row lists size p, size m, size q and distance
d. The columns are M2,4 M2,8 M2,12 M4,6 M4,10 M6,8 M6,12 M8,10 M10,12
Mnegsize=size(Mneg);

for i=1:Mnegsize(1)
GMD(i) = exp ( log (Mneg(i,4)) -((1./12).*(Mneg (i,4)./w).^-2) -
((1./60).*(Mneg(i,4)./w).^-4) -((1./168).*(Mneg(i,4)./w).^-6) -
((1./360).*(Mneg(i,4)./w).^-8) -((1./660).*(Mneg(i,4)./w).^-10) );

Qa = log (
((Mneg(i,1)+Mneg(i,2))./GMD(i))+(1+(((Mneg(i,1)+Mneg(i,2)).^2)./
(GMD(i).^2))).^(0.5)) - (1+( (GMD(i)).^2./(
(Mneg(i,1)+Mneg(i,2)).^2))).^(0.5)+(GMD(i)./ (Mneg(i,1)+Mneg(i,2)));
Qb = log (
((Mneg(i,2)+Mneg(i,3))./GMD(i))+(1+(((Mneg(i,2)+Mneg(i,3)).^2)./
(GMD(i).^2))).^(0.5)) - (1+( (GMD(i)).^2./(
(Mneg(i,2)+Mneg(i,3)).^2))).^(0.5)+(GMD(i)./ (Mneg(i,2)+Mneg(i,3)));
Qc = log ( (Mneg(i,1)./GMD(i))+(1+(( Mneg(i,1).^2)./
(GMD(i).^2))).^(0.5)) - (1+( (GMD(i)).^2./(
Mneg(i,1).^2))).^(0.5)+(GMD(i)./ Mneg(i,1));
Qd = log ( (Mneg(i,3)./GMD(i))+(1+(( Mneg(i,3).^2)./
(GMD(i).^2))).^(0.5)) - (1+( (GMD(i)).^2./(
Mneg(i,3).^2))).^(0.5)+(GMD(i)./ Mneg(i,3));

Mn(i)= (Mneg(i,1)+Mneg(i,2)).*Qa + (Mneg(i,2)+Mneg(i,3)).* Qb -
Mneg(i,1).* Qc - Mneg(i,3).*Qd;

end
Mnegtotal=2.*(sum(Mn));              %total negative mutual inductance

Ltot= Lself + Mpostotal - Mnegtotal;            %total inductance
```